Spectral Description of Low-Frequency Oceanic Variability

XIAOYUN ZANG AND CARL WUNSCH

Department of Earth, Atmospheric, and Planetary Sciences, Massachusetts Institute of Technology, Cambridge, Massachusetts

(Manuscript received 15 May 2000, in final form 6 April 2001)

ABSTRACT

A synthesis is made of simple dynamics with a wide variety of observations to produce a zero-order approximate analytical spectral description of low-frequency oceanic variability in the Northern Hemisphere oceans. Because the spatial inhomogeneity is so great, one must account for it at lowest order, rendering a power density spectrum only a first step toward to a full statistical description. The fundamental hypothesis is that there exists, for each vertical mode of variability, n, a function $\Phi(k, l, \omega, n, \phi, \lambda)$, where (k, l) are local horizontal wavenumbers; ω is frequency; and (ϕ, λ) are latitude and longitude, respectively, and that can, as a first approximation, be represented in a simple factored form. Data from altimetry, moored current and temperature sensors, acoustic tomography, and XBTs are used to find a first guess form for $\Phi(k, l, \omega, n, \phi, \lambda)$, which is at least semiquantitatively accurate. A useful model spectrum proves to be representable as a product of separate factors for wavenumber, frequency, mode number, and a function of latitude and longitude. The results raise dynamical questions concerning the forms that emerge, and present a challenge for improvement of the representation by existing and future observations. Numerous improvements can be made to the detailed structure. A number of illustrative applications are then made, including calculation of an unobserved spectrum (velocity wavenumber) and the detection of climate-scale shifts in ocean property fluxes.

1. Introduction

Over the past several decades, the oceanographic community has acquired a large variety of measurements of oceanic variability. This variability depends on the data type (e.g., sea level, velocity at depth), time and space scales, and the location. The details lie in many millions of separate measurement values. One is led to ask whether there are some simple analytical descriptors of the many data that would permit one to unify what is otherwise a bewildering amount of detail.

The synthesis of internal waves by Garrett and Munk (1972, hereafter GM) revolutionized that field by showing that a comparatively simple set of rules described the seemingly highly disparate results. Their spectral density estimate led to an explosion in knowledge of internal waves, both observationally and in stimulating theoretical work to understand the particular descriptive rules. We are motivated by the success of that effort to ask whether an analogous set of rules exist for oceanic variability at frequencies lower than the local inertial frequency. From the existing literature on oceanic variability, one expects, a priori, a much more difficult task: GM were able to assume temporal and spatial stationarity (homogeneity) and lateral and vertical isotropy. None of these assumptions can be expected to be valid at lower frequencies, and it is not at all obvious whether an analogous synthesis is possible.

Our working definition of ''low frequency variability'' is motions on timescales longer than the inertial period and shorter than a few years, and with spatial scales ranging from tens to thousands of kilometers. Theoretically, there is no low-frequency cutoff for periods shorter than the lifetime of the ocean, but because most observations span only months to a year or two, we leave the description of very low-frequency motions (beyond a year or two) to the future. A long wavelength cutoff does exist, given by the circumference of the earth, which is nearly 40 000 km. Again, the practicalities of array dimensions, and the very strong inhomogeneities associated with boundary currents, limit us in practice to the oceanic interior and to longest wavelengths of about 1000 km. This scale is sufficiently short that to the extent that we find the spatial inhomogeneity is on yet longer scales, we will be making a two-scale approximation: a locally uniform spectrum is modulated by a slowly changing geographical function. For a zero-mean stationary Gaussian process, it is easy to show that the power density spectrum is a complete statistical specification [Gille and Llewellyn-Smith (2000) show that altimetric velocity data are at least locally indistinguishable from Gaussian].

For technical purposes however, the energy on wavelengths longer than 1000 km cannot be ignored completely, both because the observed spectrum of sea sur-

Corresponding author address: Dr. Xiaoyun Zang, Department of Earth, Atmospheric, and Planetary Sciences, Massachusetts Institute of Technology, Cambridge, MA 02139.
E-mail: xiaoyun@pimms.mit.edu

face height on long wavelengths is slightly red between about 400 km and the longest possible wavelength and we need to suppress Gibbs effects, which would otherwise be present in the corresponding covariance functions. In this study, the wavenumber spectral structure at wavelengths longer than 1000 km and shorter than 40 000 km is derived in part by extrapolation.

The equatorial waveguide is considered here to be a boundary region, and is not explicitly described. Mixed layer motions and surface temperature variations also lie beyond the scope of the dynamics used. Despite these limitations, a successful spectral description could still apply to most of the volume of the world ocean.

2. Dynamic model for low frequency motion

We take as our basic model, the linearized β plane, equations (e.g., Gill 1982) for perturbation quantities and adopt the conventional definitions of u, v, w, ρ, and p. Separating variables,

$$p(x, y, z, t) = \sum_{n=0}^{\infty} p_n(x, y, z, t) = \sum_{n=0}^{\infty} P_n(x, y, t)F_n(z), \quad (1)$$

leads to a sum over orthonormal vertical modes, $F_n(z)$, satisfying (Gill 1982):

$$\frac{d}{dz}\left(\frac{1}{N^2(z)}\frac{dF_n(z)}{dz}\right) = -r_n^2 F_n(z), \quad (2)$$

where r_n^2 is a separation constant.

Here, $w(z)$ is proportional to another vertical mode function, $G_n(z)$:

$$G_n(z) = \frac{1}{N^2(z)}\frac{dF_n(z)}{dz}, \quad (3)$$

where

$$\frac{d^2G_n(z)}{dz^2} + r_n^2 N^2(z)G_n(z) = 0. \quad (4)$$

Equations (2) and (4) are readily solved numerically. Analytic solutions to the vertical equation are available for a few forms of $N(z)$, including the exponential profile,

$$N(z) = N_0 e^{az}, \quad (5)$$

which following GM, we will adopt for use over the whole depth with $N_0 = 0.007\ \mathrm{s}^{-1}$ and $a = 0.001\ \mathrm{m}^{-1}$ in dimensional form. Equation (5) is a reasonable fit to the actual buoyancy profile below 1 km. Use of a regionally varying form, perhaps with arbitrary vertical structure, is one of the ways in which the results below could be improved. Here the relative insensitivity of F_n, G_n to details of $N(z)$ is exploited.

Observations strongly suggest the presence of vertical standing modes for low frequency variability. Given the exponential profile of $N(z)$ and vertical boundary conditions, Eqs. (2) and (4) can be solved analytically. The solutions of the vertical eigenvalue problem are given in appendix A.

The Rossby radius of deformation for mode n can be obtained from r_n through

$$R_n = \frac{1}{fr_n}. \quad (6)$$

The first four eigenvalues, r_n, are listed in Table 1 and can be compared to the values from climatology of Chelton et al. (1998).

The horizontal structure for each mode is represented in the form of propagating waves:

$$P_n(x, y, t) = \int_{-\infty}^{+\infty}\int_{-\infty}^{+\infty}\int_{-\infty}^{+\infty} \tilde{p}(k, l, \omega, n)e^{i2\pi(kx+ly-\omega t)}\, dk\, dl\, d\omega, \quad (7)$$

where (k, l) are the local horizontal wavenumbers and ω is the frequency. Cyclical frequencies and wavenumbers are used here. The full solution for each mode, in pressure, is

$$p_n(x, y, z, t) = \int_{-\infty}^{+\infty}\int_{-\infty}^{+\infty}\int_{-\infty}^{+\infty} \tilde{p}(k, l, \omega, n)F_n(z)e^{i2\pi(kx+ly-\omega t)}\, dk\, dl\, d\omega. \quad (8)$$

Define

$$\tilde{\psi}(k, l, \omega, n) = \frac{\tilde{p}(k, l, \omega, n)}{\rho_0 f}, \quad (9)$$

which represents the Fourier transform of the streamfunction for each mode. If the signal is real $\tilde{\psi}^*(k, l, \omega, n) = \tilde{\psi}(-k, -l, -\omega, n)$, where the asterisk denotes the complex conjugate.

At low frequencies, given the streamfunction ψ_n, horizontal velocity can be derived through the geostrophic relations, and density and vertical velocity can be obtained from the hydrostatic equation and density conservation equation, respectively. Let $q_n(x, y, z, t)$ be a generic variable for the nth mode, that is, any one of the dependent variables $p_n(x, y, z, t)$, $u_n(x, y, z, t)$, etc. Then, for any variable,

$$q_n(x, y, z, t) = \int_{-\infty}^{+\infty}\int_{-\infty}^{+\infty}\int_{-\infty}^{+\infty} \tilde{\psi}(k, l, \omega, n)\tilde{q}(k, l, \omega, n)e^{i2\pi(kx+ly-\omega t)}\, dk\, dl\, d\omega, \quad (10)$$

where $\tilde{q}$ is the characteristic function for each of the dependent variables. The specific characteristic functions for pressure, zonal velocity, temperature, etc., are provided in appendix B.

3. Spectra of the model

We begin by working with the individual vertical modes.

a. Covariance and cross-covariance

For a spatially and temporally stationary process,

$$\langle\tilde{\psi}(k, l, \omega, n)\tilde{\psi}^*(k', l', \omega', n)\rangle = \delta(k'-k)\delta(l'-l)\delta(\omega'-\omega)\langle|\tilde{\psi}(k, l, \omega, n)|^2\rangle, \quad (11)$$

where the angle bracket represents an ensemble average. Define

$$\Phi(k, l, \omega, n) = \langle|\tilde{\psi}(k, l, \omega, n)|^2\rangle, \quad (12)$$

which is the three-dimensional frequency and wavenumber spectrum of the streamfunction for each vertical mode. For a real signal, $\Phi(-k, -l, -\omega, n) = \Phi(k, l, \omega, n)$. The autocovariance function of $q_n(x, y, z, t)$ is

$$R_q(r_x, r_y, \tau, z, n) = \int_{-\infty}^{+\infty}\int_{-\infty}^{+\infty}\int_{-\infty}^{+\infty} \tilde{q}(k, l, \omega, z, n)\tilde{q}^*(k, l, \omega, z, n)\Phi(k, l, \omega, n)e^{-i2\pi(kr_x+lr_y-\omega\tau)}\, dk\, dl\, d\omega. \quad (13)$$

Let $s_n(x, y, z, t)$ be any other generic variable; then the cross-covariance function between $q_n(x, y, z, t)$ and $s_n(x, y, z, t)$ for a homogeneous and stationary process is

$$R_{qs}(r_x, r_y, \tau, z, n) = \int_{-\infty}^{+\infty}\int_{-\infty}^{+\infty}\int_{-\infty}^{+\infty} \tilde{q}(k, l, \omega, z, n)\tilde{s}^*(k, l, \omega, z, n)\Phi(k, l, \omega, n)e^{-i2\pi(kr_x+lr_y-\omega\tau)}\, dk\, dl\, d\omega. \quad (14)$$

b. Three-dimensional spectra

The three-dimensional spectra of q for fixed z are

$$\Upsilon_q(k, l, \omega, z, n) = |\tilde{q}|^2\Phi(k, l, \omega, n). \quad (15)$$

If the full three-dimensional spectrum of any variable for each mode were known, $\Phi(k, l, \omega, n)$ could be obtained from (15) from any q, but no such spectrum has ever been determined. We must resort to various estimates of one- and two-dimensional projections of Υ and attempt to estimate the underlying three-dimensional structure.

Notation is a problem. We will use a superscript (1), (2) to denote the dimensionality (apart from z, n) of the spectrum, but must ask the reader to recognize that changing arguments denote different functions. So for example, $\Upsilon_q^{(2)}(k, l, z, n)$ is a different function from $\Upsilon_q^{(2)}(k, \omega, z, n)$. Otherwise, the notation list becomes unworkable.

TABLE 1. Eigenvalue, gravity-wave phase speed, and equivalent depth.

Mode number	Eigenvalue (r_n) (s m^{-1})	Gravity-wave phase speed (c_n) (m s^{-1})	Equivalent depth (h_n) (cm)
0	0	∞	∞
1	0.402	2.48	63
2	0.861	1.16	14
3	1.319	0.76	6

c. Two-dimensional spectra

Two-dimensional spectra are

$$\Upsilon_q^{(2)}(k, l, z, n) = \int_{-\infty}^{+\infty} |\tilde{q}|^2\Phi(k, l, \omega, n)\, d\omega, \quad (16)$$

$$\Upsilon_q^{(2)}(k, \omega, z, n) = \int_{-\infty}^{+\infty} |\hat{q}|^2\Phi(k, l, \omega, n)\, dl, \quad (17)$$

etc.

d. One-dimensional spectra

The one-dimensional frequency spectra are

$$\Upsilon_q^{(1)}(\omega, z, n) = \int_{-\infty}^{+\infty}\int_{-\infty}^{+\infty} |\tilde{q}|^2\Phi(k, l, \omega, n)\, dk\, dl \quad (18)$$

and the wavenumber k spectra are

$$\Upsilon_q^{(1)}(k, z, n) = \int_{-\infty}^{+\infty}\int_{-\infty}^{+\infty} |\tilde{q}|^2 \Phi(k, l, \omega, n)\, dl\, d\omega, \quad (19)$$

and analogously for all others.

e. Energy level

The kinetic energy for each mode at depth z is

$$E_k(z, n) = \frac{1}{2}\int_{-\infty}^{+\infty}\int_{-\infty}^{+\infty}\int_{-\infty}^{+\infty} (|\tilde{u}|^2 + |\tilde{v}|^2)\Phi(k, l, \omega, n)\, dk\, dl\, d\omega,$$

and the kinetic energy per unit surface area is

$$K_E(n) = \int_{-h}^{0} E_k(z, n)\, dz. \quad (20)$$

The potential energy per unit surface area is

$$P_E(n) = \frac{1}{2}\int_{-\infty}^{+\infty}\int_{-\infty}^{+\infty}\int_{-\infty}^{+\infty}\int_{-h}^{0} N^2|\tilde{\zeta}|^2\Phi(k, l, \omega, n)\, dz\, dk\, dl\, d\omega.$$

The rigid-lid assumption has very little effect on the eigenvalues and eigenfunctions of baroclinic modes; its effect on the potential energy of baroclinic modes can be ignored. For barotropic motions, the free surface is important only for waves with wavelengths greater than about 2000 km. The potential energy contribution from the barotropic mode is set to zero here.

f. Heat and momentum transport

For this linear model,

$$\langle u_n\theta_n\rangle = \langle v_n\theta_n\rangle = 0, \quad (21)$$

and there is no eddy heat transport. Wunsch (1999a) estimated the eddy heat fluxes based on quasi-global current meter and temperature mooring records. He concluded that eddy heat fluxes were generally quite small with respect to total heat fluxes in the ocean interior and only significant near western boundary current areas and in the Southern Ocean so that (21) is not a crippling assumption.

The momentum transport is

$$\langle u_n v_n\rangle = R_{uv}(0, 0, 0, z, n) = -F_n^2(z)\int_{-\infty}^{+\infty}\int_{-\infty}^{+\infty}\int_{-\infty}^{+\infty} 4\pi^2 kl\Phi(k, l, \omega, n)\, dk\, dl\, d\omega,$$

which vanishes only if $\Phi(k, l, \omega, n)$ is isotropic.

4. Observed spectra

a. A First-guess k, l, ω spectral form

The simplest form is one that factors, and we postulate as a working hypothesis,

$$\Phi(k, l, \omega, n, \phi, \lambda) = B_n(k)C_n(l)D_n(\omega)E_0(n)I(\phi, \lambda). \quad (22)$$

Here $B_n(k)$ and $C_n(l)$ are the zonal- and meridional-wavenumber spectral densities of nth mode respectively; $D_n(\omega)$ is the corresponding frequency spectrum; $E_0(n)$ is a constant determining the energy partition among modes; and $I(\phi, \lambda)$ is a slowly varying spatial function. [As discussed by Zang (2000), the frequency and wavenumber separated form in (22) does not distinguish westward- from eastward-going energy. A more sophisticated frequency and wavenumber coupled form for $\Phi(k, l, \omega, n, \phi, \lambda)$ is eventually required to represent these effects.]

b. Horizontal inhomogeneity

The most striking property of low frequency kinetic energy is the variation of energy level with position. Figure 1a (Wunsch 1997) shows surface kinetic energy from the current meters in the North Pacific; Fig. 1b (Stammer 1997) displays the surface kinetic energy from the altimeter in the North Pacific. There is rough agreement between the two estimates. The corresponding estimates in the North Atlantic are shown in Fig. 2.

The zonal averages between 0° and 360°E of surface eddy kinetic energy E_k and sea surface slope variance $V_{sl} = E_k \sin^2\phi$ are provided as a function of latitude in

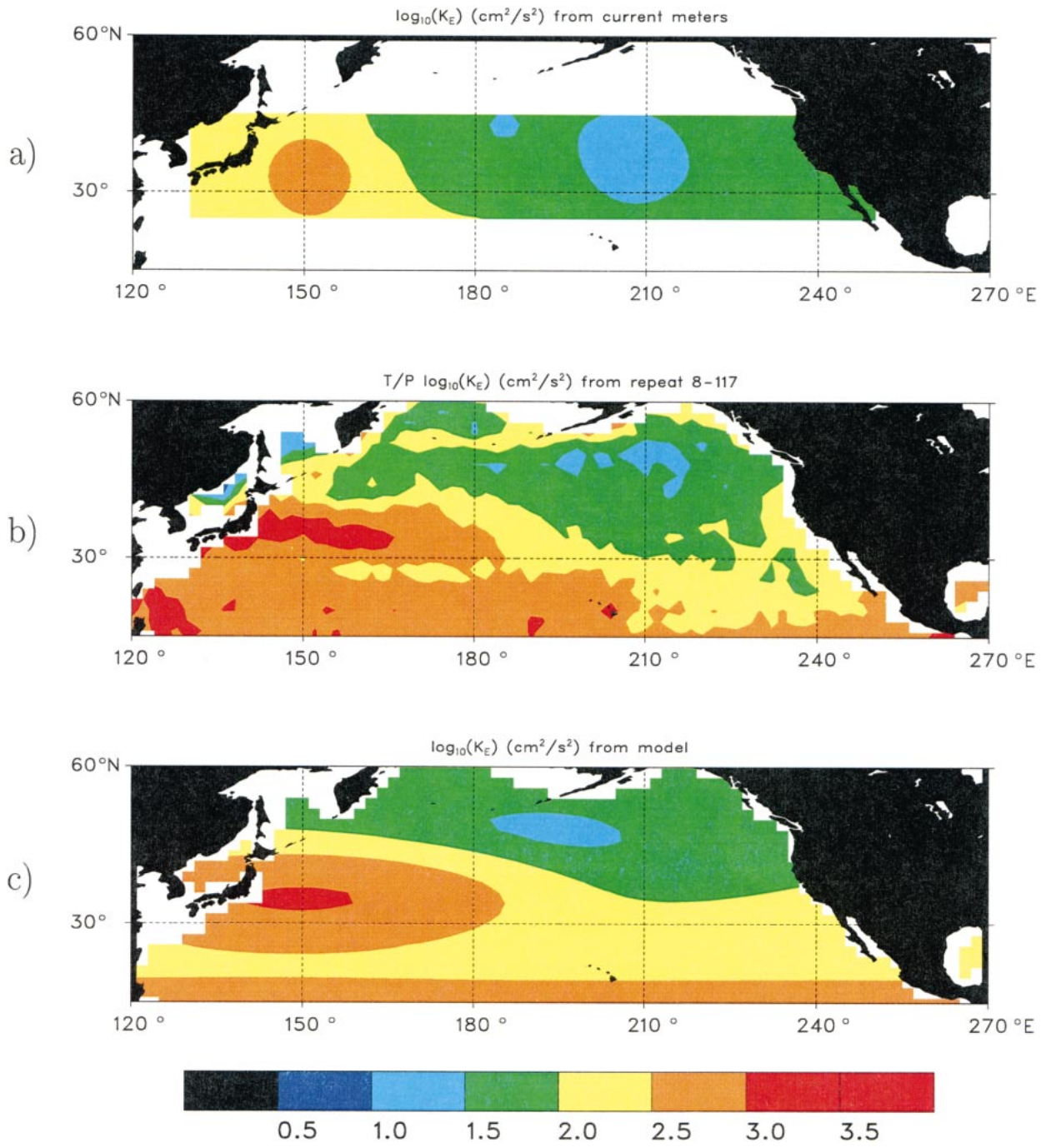

FIG. 1. Surface eddy kinetic energy in the region of North Pacific. (a) from the current meters (Wunsch 1997), (b) from TOPEX/Poseidon data (Stammer 1997), and (c) from the empirical formula.

Fig. 3 (Stammer 1997). The zonally averaged E_k decreases from a maximum near the equator to a minimum in high latitudes. Between 25°S and 25°N V_{sl} remains almost constant. So equatorward of 25°, the zonally averaged E_k is approximately inversely proportional to $\sin^2\phi$.

We represent the surface eddy kinetic energy in the North Pacific as the sum of four parts: 1) a uniform background, 2) a low latitude component (south of the energetic currents) where $E_k \propto (1/\sin^2\theta)$, 3) a high energy region with a center near (35°N, 150°E), and 4) a low energy area in the north North Pacific and expressed as

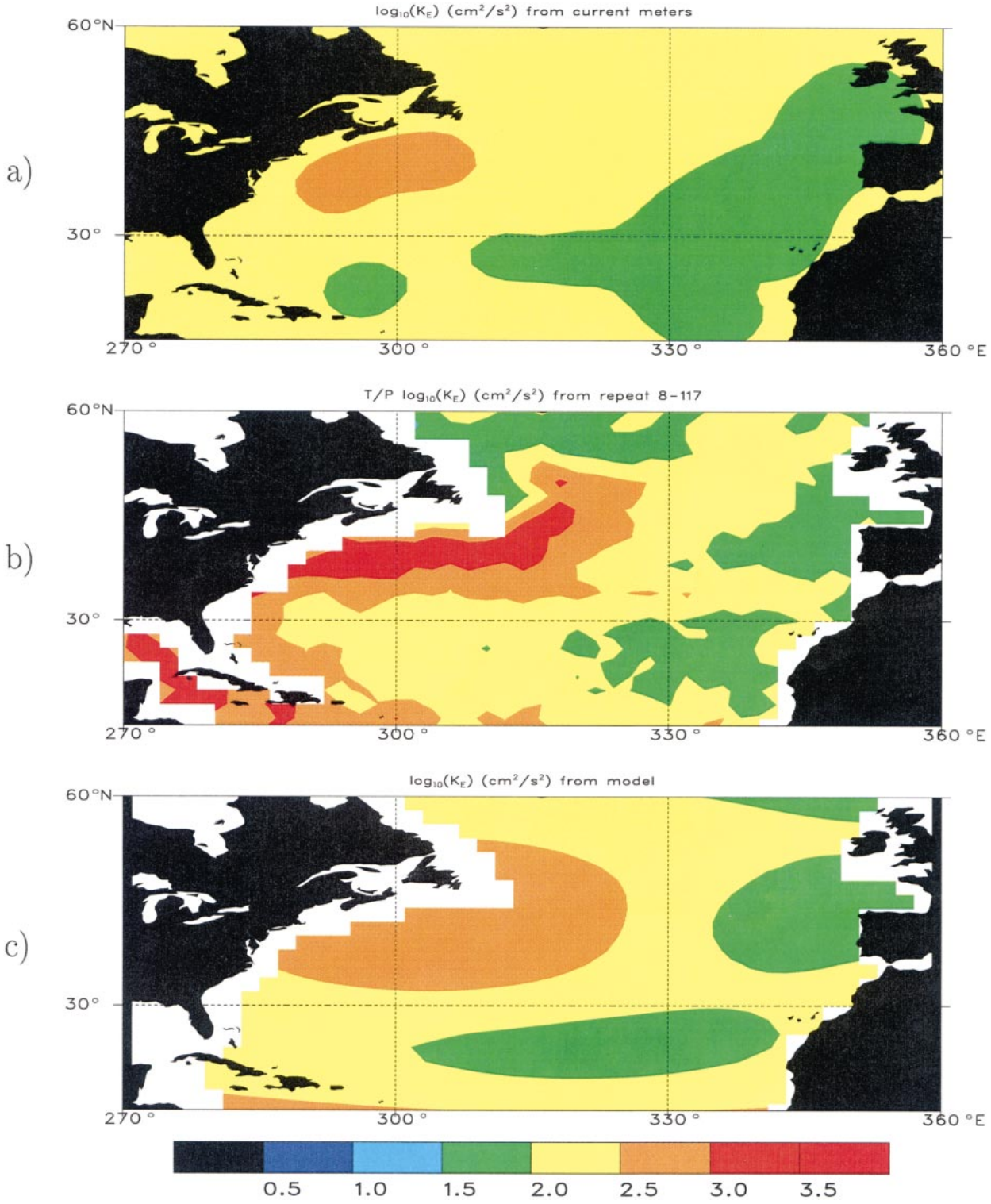

FIG. 2. As in Fig. 1 except for North Atlantic.

$$E_{kP}(\phi, \lambda, z = 0) = 0.003 + \frac{0.0032}{\sin^2\phi} + 0.1 \exp\left\{-\left[\frac{(\lambda - 150)^2}{900} + \frac{(\phi - 35)^2}{50}\right]\right\} - 0.008 \exp\left\{-\left[\frac{(\lambda - 190)^2}{1600} + \frac{(\phi - 42)^2}{200}\right]\right\}, \quad 120° \le \lambda \le 270°\text{E}, \quad 10° \le \phi \le 60°\text{N} \tag{23}$$

in units of $m^2\ s^2$. For the North Atlantic, the corresponding expression is

$$E_{kA}(\phi, \lambda, z = 0) = 0.005 + \frac{0.0035}{\sin^2\phi} + 0.1 \exp\left\{-\left[\frac{(\lambda - 305)^2}{400} + \frac{(\phi - 43)^2}{80}\right]\right\} - 0.028 \exp\left\{-\left[\frac{(\lambda - 320)^2}{2000} + \frac{(\phi - 16)^2}{200}\right]\right\} - 0.016 \exp\left\{-\left[\frac{(\lambda - 320)^2}{900} + \frac{(\phi - 42)^2}{50}\right]\right\}, \quad 280° \le \lambda \le 360°\text{E}, \quad 10° \le \phi \le 60°\text{N}. \tag{24}$$

The expressions (23) and (24) were obtained by inspection. Results from Eqs. (23) and (24) are shown in Figs. 1c and 2c, respectively, and are generally within a factor of 2 of the observations everywhere. It remains to determine $B_n(k)$, $C_n(l)$, $D_n(\omega)$, and $E_0(n)$.

c. Vertical structure of kinetic energy and potential energy

Schmitz (1978, 1988) showed that to a first approximation the vertical profile of eddy kinetic energy was independent of geography across the entire midlatitude band. Eddy kinetic energy, E_k, dropped exponentially from the surface to a depth of about 1200 m, then remained almost constant within the abyss.

Wunsch (1997) showed that in the open North Pacific, about 30%–40% of the water column average kinetic energy was in the barotropic mode and about 55% was in the first baroclinic mode. The open North Atlantic has about 40% of the kinetic energy in the barotropic and 50% in the first baroclinic modes. Strong deviations from these values occur near the Gulf Stream and near the equator, and no attempt is made here to model them in those regions. The results by Wunsch and Schmitz are consistent: because the first baroclinic mode is surface intensified, horizontal kinetic energy will be dominated by the first baroclinic mode in the upper ocean; thus it will decay nearly exponentially in the main thermocline. Within the deep water, horizontal kinetic energy remains almost constant because the deep ocean is dominated by the barotropic mode. These results are all reduced to the statement, for present purposes, that the vertically integrated modal energies are in the ratio 1: 1:1/2 for the barotropic through the second baroclinic modes.

Wunsch (1999b) inferred the vertical displacement of an isopycnal from temperature measurements and investigated the vertical structure of potential energy in the North Atlantic. He found that 30%–40% of the water column average potential energy was in the first baroclinic mode. The ratio of kinetic energy in the first baroclinic mode to potential energy was 0.2–0.4 in midlatitudes away from the western boundary.

d. Observed spectra of sea surface height

Pressure perturbations at the sea surface are related to elevation changes through

$$p(x, y, z = 0, t) = gp\eta(x, y, t), \tag{25}$$

which is correct even with the rigid-lid assumption. Equation (25) has been used to estimate the spectrum of p (Stammer 1997; Wunsch and Stammer 1998). However, the vertical partitioning of the modes generating the surface pressure fluctuations must be inferred independently. Zang (2000) further investigated the spectral dependence on zonal- and meridional-wavenumber and frequency. As a representative result, Figs. 4 and 5 show the zonal-wavenumber and frequency spectrum of sea surface height in the area 26°–50°N, 195°–225°E in the North Pacific. The wavenumber spectrum spectral slope is about $-1/2$ at wavelengths longer than 400 km, increasing to about -2.5 at shorter wavelengths. Zang (2000) found that the meridional-wavenumber spectrum is very similar to the zonal-wavenumber spectrum. The spectrum in Fig. 4 has a similar shape to the globally averaged one, which can be written (Wunsch and Stammer 1995)

$$\Upsilon_{\eta}^{(1)}(k) \propto \begin{cases} |k|^{-1/2}, & 1/40\,000 \le |k| \le 1/400 \text{ (cycles per km)} \\ |k|^{-5/2}, & 1/400 \le |k| \le 1/150 \text{ (cycles per km)} \\ |k|^{-4}, & 1/150 \le |k|. \end{cases} \tag{26}$$

The frequency spectrum in Fig. 5 is dominated by the seasonal cycle; the peak near 60 days is a residual tidal alias. On timescales shorter than about 100 days, the

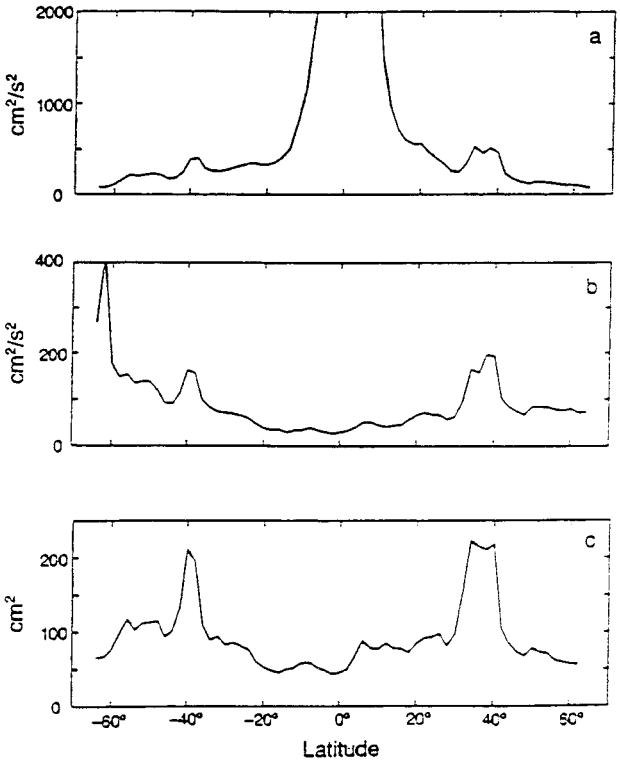

FIG. 3. Zonal averages between 0° and 360°E of (a) E_k, (b) V_{sl}, and (c) sea surface height variance plotted vs latitude (Stammer 1997).

spectra approximately follow an ω^{-2} power law, with an $\omega^{-1/2}$ form at longer periods. Stammer (1997) compared the wavenumber and frequency spectra in different regions and found them to be nearly uniform in shape in the extratropical basins. Uncertainty remains at wavelengths shorter than about 100 km because measurements by TOPEX/Poseidon at high wavenumbers are contaminated by noise and aliasing by small-scale physical processes such as internal waves and internal tides (Wunsch and Stammer 1995).

e. Observed wavenumber spectra of temperature

The data used here are from the repeated XBT lines in the North Pacific between San Francisco and Hawaii and extend to 800 m. They were previously compared to TOPEX/Poseidon data by Gilson et al. (1998), who found that at wavelengths longer than about 500 km, altimetric height variability has a coherence with steric height of 0.9. The time-averaged wavenumber spectra of the temperature perturbations at different depths are displayed in Fig. 6 with a spectral shape nearly independent of depth; this result at least partially justifies the assumption that the modal partition is independent of wavenumber. The temperature wavenumber spectrum obtained by Roemmich and Cornuelle (1990) in the South Pacific has nearly identical form.

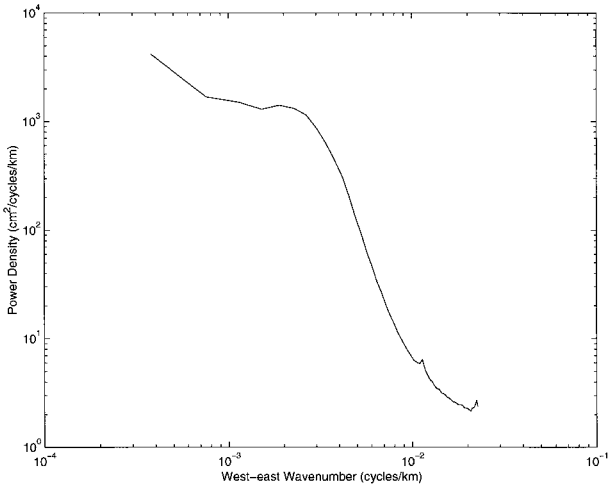

FIG. 4. Zonal wavenumber spectrum of sea surface height from TOPEX/Poseidon and *ERS-1/2* altimeter measurements (Le Traon et al. 1998).

The wavenumber spectral shape of temperature is almost identical to that of surface elevation with a breakpoint near 400 km. The similarities of sea-surface height and interior temperature spectra and the latter's apparent depth independence permit a straightforward combination of the two very different data types.

f. Observed frequency spectra of horizontal velocity and temperature

Figure 7 displays the mean, frequency spectra of horizontal velocities in the barotropic and first baroclinic modes from measurements on 105 scattered current meter moorings (Wunsch 1997). At each site, the spectra have been normalized by their total energy before av-

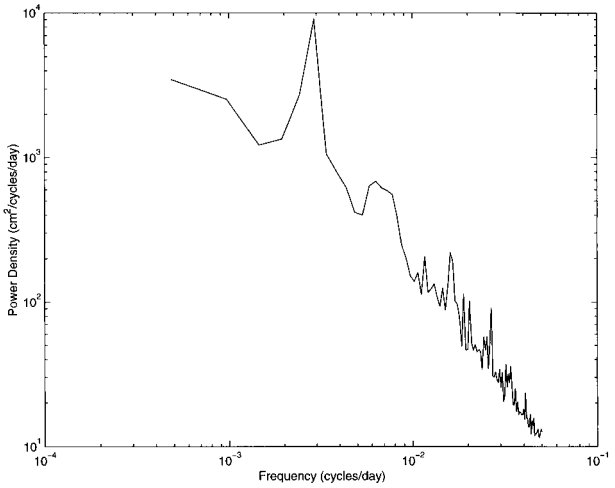

FIG. 5. Frequency spectrum of sea surface height from TOPEX/Poseidon and *ERS-1/2* altimeter measurements (Le Traon et al. 1998). The conspicuous peak is from the annual cycle and a much smaller peak near the 60-day period is a small residual tidal alias.

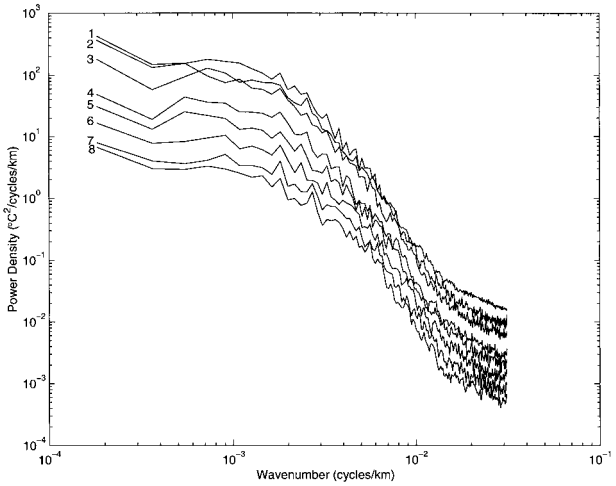

FIG. 6. Wavenumber spectra of temperature from XBT measurements (Gilson et al. 1998) averaged among depths (1) 0–100 m, (2) 100–200 m, . . . , (8) 700–800 m.

eraging. The results for zonal and meridional velocities in the barotropic and first baroclinic mode are very similar. As will be seen later, in most regions the flows are isotropic, in the sense that the difference between the frequency spectra of the two components of horizontal velocity is statistically insignificant. Frequency spectra of the barotropic and first baroclinic mode also display similar structure, implying that the frequency spectral shape of horizontal velocity is again, to first order, independent of depth and is basically universal in shape. Variance-preserving figures (not shown) demonstrate that the kinetic energy is dominated by motions with periods around 100 days—the mesoscale.

Moored temperature frequency spectra (e.g., Fig. 8) are not very dependent on geography either and exhibit a behavior similar to that of velocity. Away from major topographic features, these are also essentially independent of depth. But the energy level of the temperature frequency spectra drops more rapidly with depth than that of the horizontal velocity and is a consequence of the reduction in the vertical temperature gradient with depth.

g. Acoustic tomography data

Tomographic data integrate spatially through the ocean, thus filtering out high wavenumbers. Assuming that a preliminary inversion of the data has been done, tomographic observations are reduced to a horizontal average of temperature at fixed depths (Munk et al. 1996).

Suppose the acoustic ray path is along the east–west direction and the equivalent horizontal tomographic path length is L. Then it is readily shown that the frequency spectral density of the tomographic temperature average is

$$\Upsilon_d(\omega, z, n) = \int_{-\infty}^{+\infty}\int_{-\infty}^{+\infty} |\tilde{\theta}|^2 \Phi(k, l, \omega, n) W(k, L)\, dk\, dl, \quad (27)$$

where

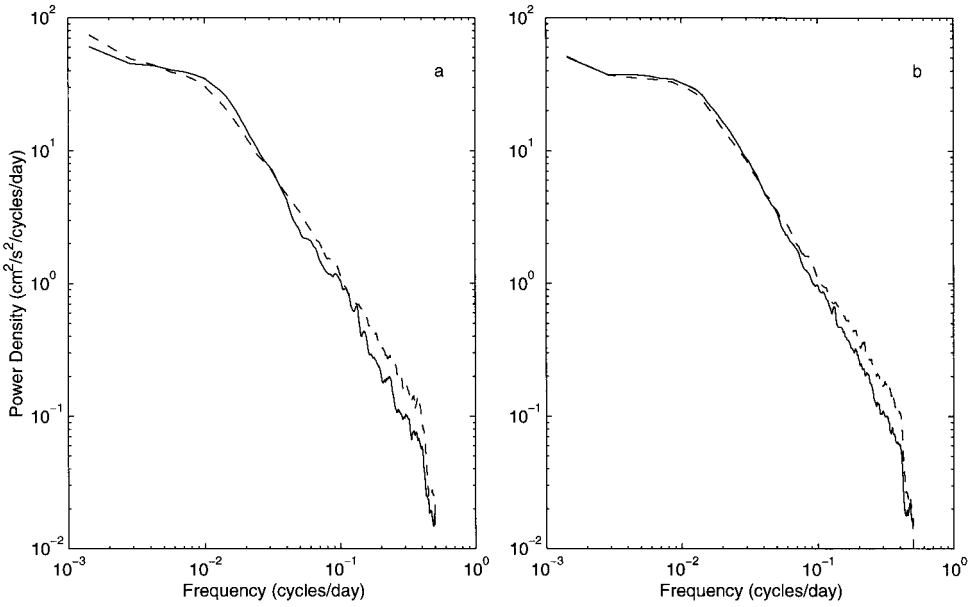

FIG. 7. Estimated mean normalized frequency spectra of zonal (a) and meridional (b) velocities in the barotropic (solid line) and first baroclinic modes (dashed line) from 105 current meter measurements (Wunsch 1997). At each site, the spectra have been normalized by their total energy before the spatial average is done.

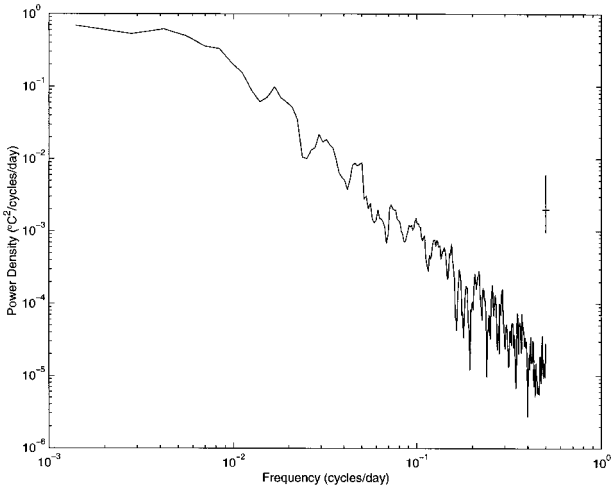

FIG. 8. Frequency spectrum of temperature at the depth of 635 m at 41.0°N, 185°E (Wunsch 1997). The spectrum is estimated using the multitaper method (Percival and Walden 1993).

$$W(k, L) = \frac{\sin^2(\pi kL)}{(\pi kL/)^2} \tag{28}$$

represents the spatial filtering. Zang (1998) analyzed the tomographic measurements from the 1987 Reciprocal Tomography Experiment and the Acoustic Thermometry of Ocean Climate. He found, as expected, that, compared with the temperature measurements at a point, tomographic data change relatively smoothly over time, because the small-scale variations have been integrated out, and that the frequency spectra of tomographic data follow an ω^{-2} power law at periods shorter than about 100 days. Equation (27) shows that if the ocean is homogeneous, the longer the acoustic ray path, the less the energy level of the frequency spectra of tomographic data. Zang (1998) found, however, that it was difficult to identify differences in energy level as a function of L in tomographic data, owing to spatial inhomogeneity, etc. But there is no conflict with Eq. (27).

h. Anisotropy

Two types of anisotropy for low frequency oceanic variability are possible: 1) The energy is not traveling uniformly in all directions. The three-dimensional spectrum of sea surface height shows that there is more energy going westward at large scales and low frequencies and the difference is about a factor of 3 in the North Pacific (Zang 2000). As mentioned above, this type of anisotropy cannot be represented by Eq. (22) and can only be modeled by a frequency and wavenumber coupled form. 2) Anisotropy is displayed in the form of differences between zonal and meridional components of horizontal velocity, which include differences in i) total energy, ii) the frequency, and iii) the wavenumber spectra. Only a very few current meter mooring array records of short duration provide direct estimates of the wavenumber spectra of velocity; these will not be discussed here (see Wunsch 1981).

Variances of the zonal and meridional components of velocity in the barotropic and first baroclinic mode from the current meter mooring measurements [see Wunsch (1997) for description of the data] were calculated for

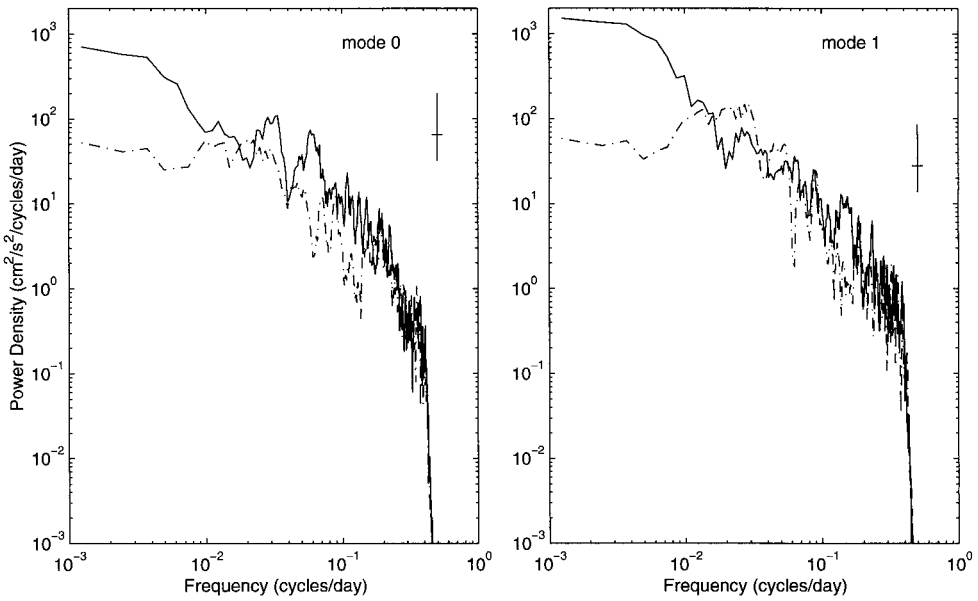

FIG. 9. Frequency spectra for the zonal (solid line) and meridional (dash–dotted line) component of horizontal velocity in the barotropic and first baroclinic mode at 38.8°N, 68.1°W (Wunsch 1997). The ratio of the variance of zonal component to that of meridional component in the barotropic and first baroclinic mode is 3.5 and 2.7, respectively.

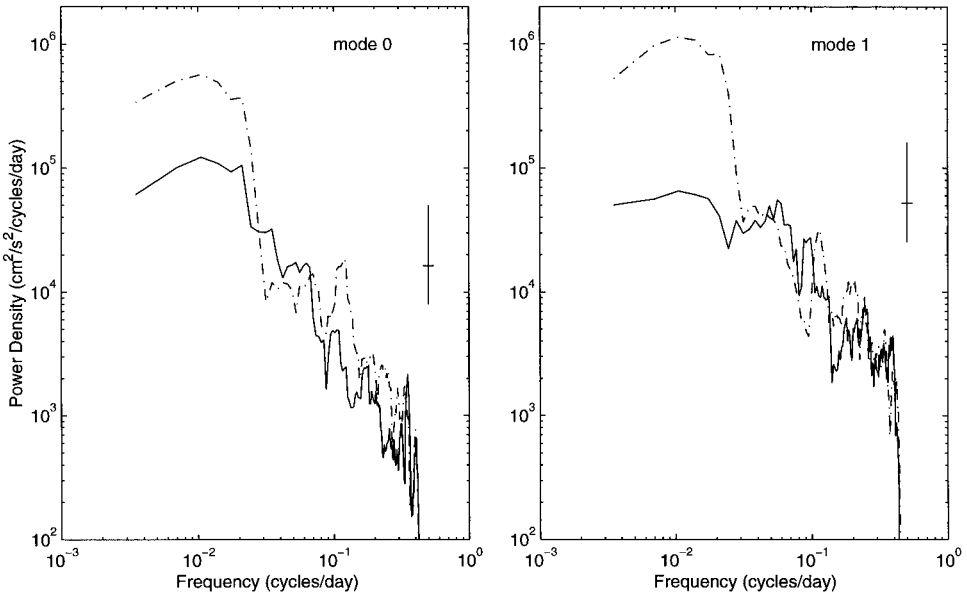

FIG. 10. As in Fig. 9 except at 38.2°N, 124.4°W (Wunsch 1997). The ratio of the variance of zonal component to that of meridional component in the barotropic and first baroclinic mode is 0.34 and 0.25, respectively.

each site. For most of them (about 80%), the difference is less than a factor of 2. For 92% of them, the difference is less than a factor of 3. Significant differences typically occur in the regions close to jets, boundaries, and fronts. At the present level of descriptive accuracy, we will ignore the differences, treating the horizontal kinetic energy as first-order isotropic. The frequency spectra of zonal and meridional components of the barotropic and first baroclinic mode at each site were then examined. Far from boundaries and strong jets, no anisotropy was found in the frequency spectra which was significant point-by-point at 95% confidence. Figures 9 and 10 present two examples of significant anisotropy. The first shows that the energy level of the frequency spectrum of the zonal component is more than an order of magnitude greater than that of the meridional component at periods longer than 100 days for both the barotropic and first baroclinic modes. The result in Fig. 10 is the opposite: at periods longer than 50 days, the energy level of the meridional component is significantly higher than that of the zonal component in the two modes. Data used in Figs. 9 and 10 were obtained from within the Gulf Stream and near the eastern boundary of the North Pacific, respectively. For the open ocean, we will thus accept the statement that the frequency spectra are indistinguishable from isotropic at all frequencies, recognizing that this is another approximation that is expected to break down in different ways near the excluded boundary areas.

*i. Fitting Φ(*k, l, ω, n, ϕ, λ*) to observations*

Because most of the region is dominated by the first few modes as described in section 4c, only the barotropic and first two baroclinic modes are included in our model: $n = 0, 1, 2$. In the following, the units of all variables are expressed in terms of meter, second, and kelvin.

For each mode,

$$\Phi(k, l, \omega, n, \phi, \lambda) = B_n(k)C_n(l)D_n(\omega)E_0(n)I(\phi, \lambda). \quad (29)$$

From the observed spectra we choose the meridional- and zonal-wavenumber spectra as

$$C_n(k) = B_n(k) = \begin{cases} 7.2 \times 10^{37}|k|^2 \\ \quad \text{if } 0 < |k| \le 2.5 \times 10^{-8} \\ 7.1 \times 10^{18}|k|^{-1/2} \\ \quad \text{if } 2.5 \times 10^{-8} < |k| \le 2.5 \times 10^{-6} \\ 4.4 \times 10^{7}|k|^{-5/2} \\ \quad \text{if } 2.5 \times 10^{-6} < |k| \le 8.0 \times 10^{-6} \\ |k|^{-4} \\ \quad \text{if } |k| > 8.0 \times 10^{-6} \quad \text{(cycles/meter).} \end{cases} \quad (30)$$

The units of $B_n(k)$ and $C_n(k)$ are 1/(cycles/meter). As described above, the finite ocean width precludes arbitrarily long wavelengths. If the spectrum at wavenumbers $0 \le |k| \le 2.5 \times 10^{-8}$ is chosen to be zero, it will be discontinuous at $|k| = 2.5 \times 10^{-8}$, and Gibbs effects will appear in the corresponding covariance functions. To minimize the Gibbs effects, the spectrum is chosen to diminish smoothly to zero from $k = 2.5 \times 10^{-8}$ to $k = 0$ by choosing it to be proportional to $|k|^2$, $0 < |k| \le 2.5 \times 10^{-8}$.

The frequency spectrum is taken to be

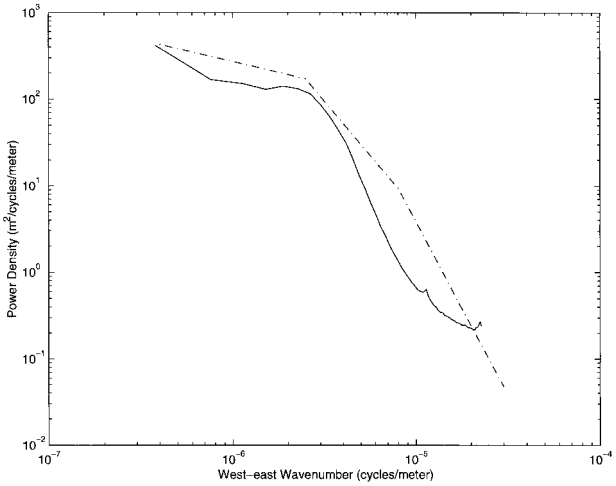

FIG. 11. Zonal-wavenumber spectrum of sea surface height. Solid line is the observed spectrum from TOPEX/Poseidon and *ERS-1/2* altimeter measurements (Le Traon et al. 1998). Dash–dotted line is the corresponding model spectrum.

$$D_n(\omega) = \begin{cases} 2.5 \times 10^{-10}|\omega|^{-1/2} \\ \quad \text{if } 0 < |\omega| \le 1.16 \times 10^{-7} \\ |\omega|^{-2} \\ \quad \text{if } |\omega| > 1.16 \times 10^{-7} \quad \text{(cycles/second)}. \end{cases} \tag{31}$$

The units of $D_n(\omega)$ are 1/(cycles/second).

The partition among vertical modes is

$$E_0(0) = 1, \qquad E_0(1) = 1, \qquad E_0(2) = 0.5, \tag{32}$$

which are nondimensional.

The magnitude function is

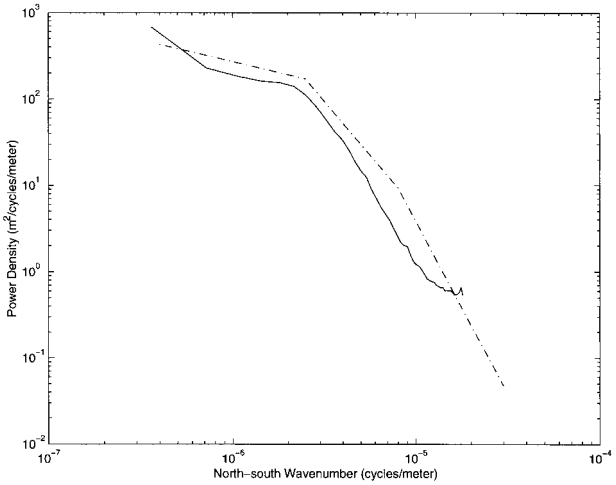

FIG. 12. Meridional-wavenumber spectrum of sea surface height. Solid line is the observed spectrum from TOPEX/Poseidon and *ERS-1/2* altimeter measurements (Le Traon et al. 1998). Dash–dotted line is the corresponding model spectrum.

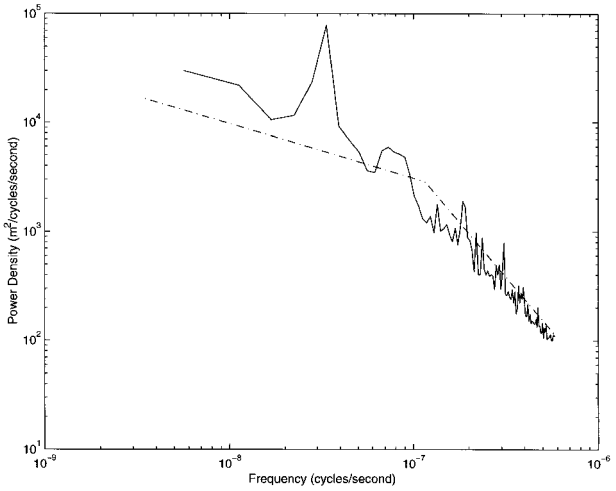

FIG. 13. Frequency spectrum of sea surface height. Solid line is the observed spectrum from TOPEX/Poseidon and *ERS-1/2* altimeter measurements (Le Traon et al. 1998). Dash–dotted line is the corresponding model spectrum. There is a striking peak at the annual period on the observed spectrum which is not modeled here. More generally, the model spectrum underpredicts the very low frequency energy by about a factor of 2.

$$I(\phi, \lambda) = \frac{E_k(\phi, \lambda, z = 0)}{8.7 \times 10^{32}}. \tag{33}$$

The units of $I(\phi, \lambda)$ are $(\text{m}^2\ \text{s}^{-2})\text{m}^2$. Expressions for $E_k(\phi, \lambda, z = 0)$ in the North Pacific and North Atlantic are in Eqs. (23) and (24), respectively.

Given $\Phi(k, l, \omega, n, \phi, \lambda)$, any spectrum of any variable at any place can be estimated. Expressions for frequency/wavenumber spectra of sea surface height, temperature, and horizontal velocity are given in appendix C, and will be used in section 5.

5. Model/data comparison

The above expressions represent the distillation of spectral estimates from very large quantities of data, and it is impractical to show all the results. But the degree to which the analytical expressions actually reproduce the underlying original spectra needs to be examined. In this section, we will display a few typical comparisons of original spectra with those inferred from (29). We will be seen to have a reasonable first description, albeit there are inevitably some misfits and discrepancies.

a. Spectra of sea surface height

The model and observed, from altimetry, zonal-wavenumber, meridional-wavenumber, and frequency spectra are plotted in Figs. 11, 12, and 13. Observed spectra are from the area of 25°–50°N, 195°–225°E described in section 4d. The energy level inside this area is relatively uniform. By (23), the average value $E_k(\phi, \lambda, z$

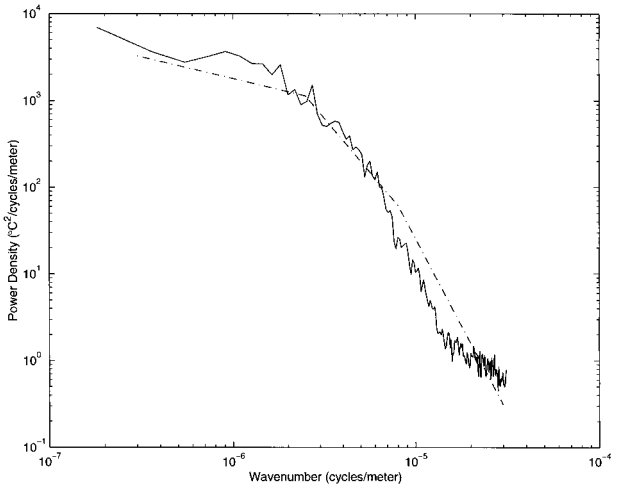

FIG. 14. Zonal-wavenumber spectrum of temperature. Solid line is the observed spectrum from XBT measurements (Gilson et al. 1998). Dash–dotted line is the corresponding model spectrum.

$= 0$) in this area is about 9.4×10^{-3} m^2 s^{-2}; therefore, $I(\phi, \lambda) = 1.1 \times 10^{-35}$ (m^2 s^{-2})m^2. Figures 11, 12, and 13 show that the model spectra are reasonable fits to the observations. One major difference between the observations and the model is that at wavelengths shorter than 200 km, the observed wavenumber spectrum is more red than the model spectrum. The reader is reminded that the gridded values used to construct the observed spectra in Fig. 11 are produced by using a spatial covariance function with correlation scale of about 200 km (Le Traon et al. 1998); this correlation partially suppresses the estimated high wavenumber spectrum.

b. Temperature wavenumber spectrum

An observed temperature wavenumber spectrum in Fig. 14 is from the XBT data in the eastern North Pacific described in section 4e, running from 38°, 236°E to 21°N, 202°E. Surface eddy kinetic energy here is relatively homogeneous, and according to (23), its mean value is about 1.5×10^{-2} m^2 s^{-2}. Because the vertical gradient of mean temperature changes strongly with location in the upper ocean, violating the assumption of horizontal homogeneity, we compare the model spectrum with the observations at the depth of 700 m; at that depth the vertical gradient of mean temperature is much more uniform. With a mean value of $\partial\theta_0/\partial z$ of about 0.0041°C/m, the model temperature wavenumber spectrum is plotted in Fig. 14 and the agreement with the observed spectrum is satisfactory.

c. Frequency spectra of horizontal velocities and temperature

Results from one set of current meter data are displayed here; the records are from 39.5°N, 232.3°E inside the low energy area in the eastern North Pacific. Record depths are nominally 160, 580, 595, 1230, 3000, and 3800 m (Wunsch 1997). Measurements at 3800 m are neglected because the temperature signals are very weak. According to (23), E_k(39.5°N, 232.3°E; $z = 0$) $= 8.6 \times 10^{-3}$ m^2 s^{-2}. Therefore, I(39.5°N, 232°E) $= 1.0 \times 10^{-35}$ (m^2 s^{-2})m^2. The vertical gradients of the mean temperature at depths of 160, 580, 595, 1230, and 3000 m are 0.020, 0.0042, 0.0040, 0.0019, and 0.00024°C/m, respectively. The model and observed spectra are plotted in Fig. 15. Visual agreement between the model and the observed spectra is again quite pleasing.

d. Ratio of kinetic energy to potential energy

The kinetic energy to potential energy ratio of the first baroclinic mode is 0.48 in midlatitudes. This value is roughly consistent with the result by Wunsch (1999b) from current meter and temperature mooring measurements (section 4c).

6. Discussion and applications

A spectral density estimate has been produced from a variety of observations restricted to regions far from oceanic boundaries and unusual topographic features, and a simplified guess at the underlying algebraic form. The model is a universal one, up to division by a geographic-dependence function $I(\phi, \lambda)$, and the resulting $\Phi(k, l, \omega, n, \phi, \lambda)/I(\phi, \lambda)$ is shown in Fig. 16. The structure of $I(\phi, \lambda)$ is completely ad hoc and is deduced primarily from the satellite altimetry in the North Atlantic and Pacific. It remains to try and construct a similar function for the other ocean basins and ultimately to understand why it takes the observed shape.

This zero-order fit fails qualitatively in the regions we have omitted, including the boundary current areas, the surface mixed layer, and the equatorial waveguide. We suspect, but cannot prove from data, that the vertical modal partition should be more heavily dominated at high frequencies (periods shorter than 10 days) by the barotropic mode. This inference is made from the behavior of recent model results (Fukumori et al. 1998; Tierney et al. 2000; Stammer et al. 2000). So few moored data exist at high latitudes that we cannot test this hypothesis with data at the present time.

To the extent that a near-universal spectrum for the open ocean emerges, one can then begin to attempt to understand why and how its structure is determined. Although a full discussion is beyond our scope, we here make some general remarks about the elements that would go into such an understanding. The low-mode character of low frequency variability is partially attributed to quasigeostrophic nonlinear interactions (two-dimensional turbulence), which drives the motion toward larger scales both in the vertical and horizontal directions (Charney 1971; Rhines 1975; Fu and Flierl

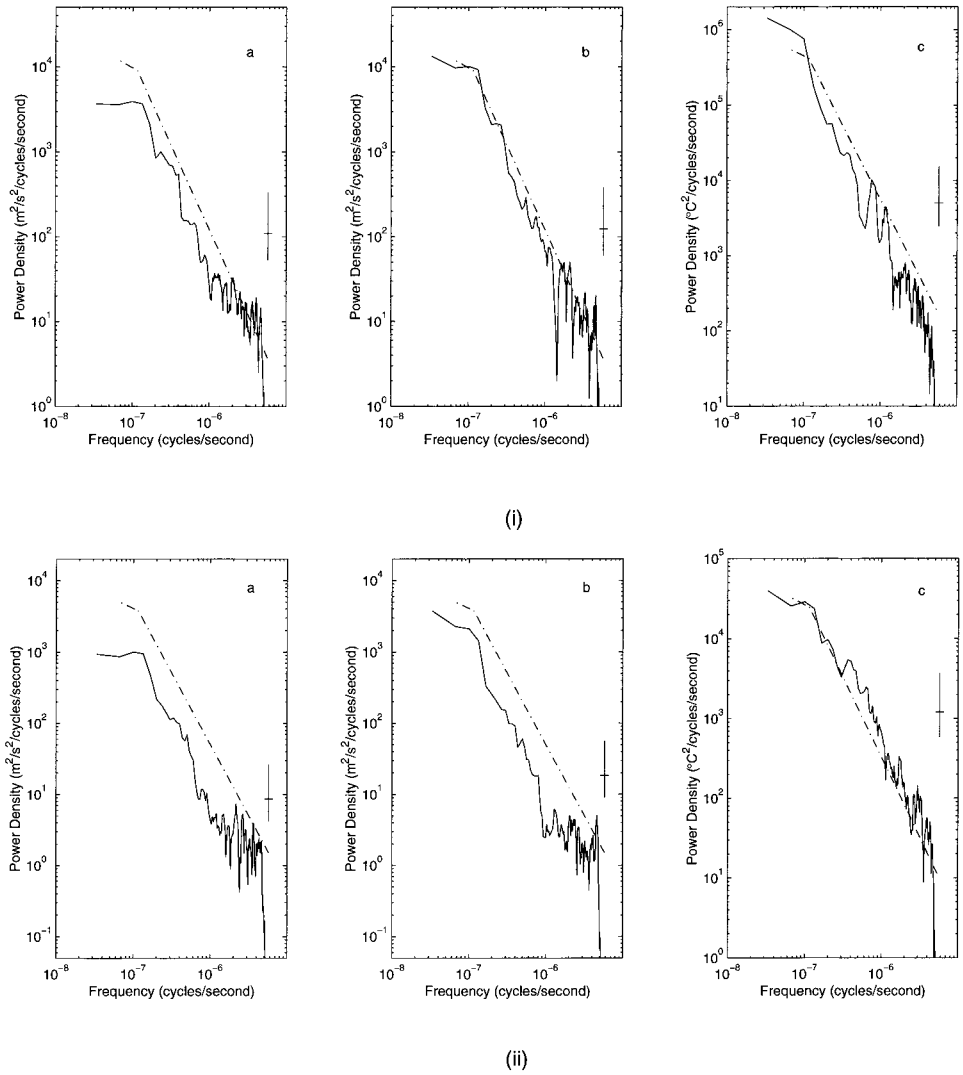

FIG. 15. Frequency spectra of zonal (a) meridional velocity (b) and, temperature (c) at depths of (i) 160 m (ii) 580 m (iii) 595 m (iv) 1230 m and (v) 3000 m. Solid line is the observed spectrum from current meter measurements (Wunsch 1997) and dash–dotted line is the model spectrum.

1979). In the absence of forcing and dissipation, two-dimensional flow must transfer kinetic energy from small to larger scales and large to smaller scales through nonlinear interactions between different scales of motion (Fjortoft 1953). Kraichnan (1967) postulated that there exists two distinct ''inertial'' subranges of two-dimensional turbulence. The large-scale subrange has a kinetic energy spectrum of $k^{-3/5}$, while the kinetic energy spectrum of small-scale subrange is proportional to k^{-3}. Charney (1971) also obtained a -3 law at the tail of the kinetic energy spectrum from a quasigeostrophic model and conjectured that in this region there would be equipartition between the kinetic and potential energies.

Rhines (1975) further argued that kinetic energy should exhibit a maximum at the wavelength close to the scale, $l \propto \sqrt{U/\beta}$, where U is a measure of the ambient velocity. Results from numerical simulation are consistent (Lilly 1969; McWilliams and Chow 1981) with that argument. For the ocean, two-dimensional turbulence theory only offers explanations for the spectral shape at wavelengths smaller than about 400 km. It is unclear why the wavenumber spectra of sea surface height and temperature are proportional to $k^{-1/2}$ at wavelengths longer than 400 km. In a full turbulence theory, one would have a connection between frequency and wavenumber structure; no such relationship is known to us for the ocean.

The frequency spectral shape can be rationalized in part as the integral response of the ocean to continuous random forcing of the atmosphere (Hasselmann 1976; Frankignoul and Hasselmann 1977). They showed a

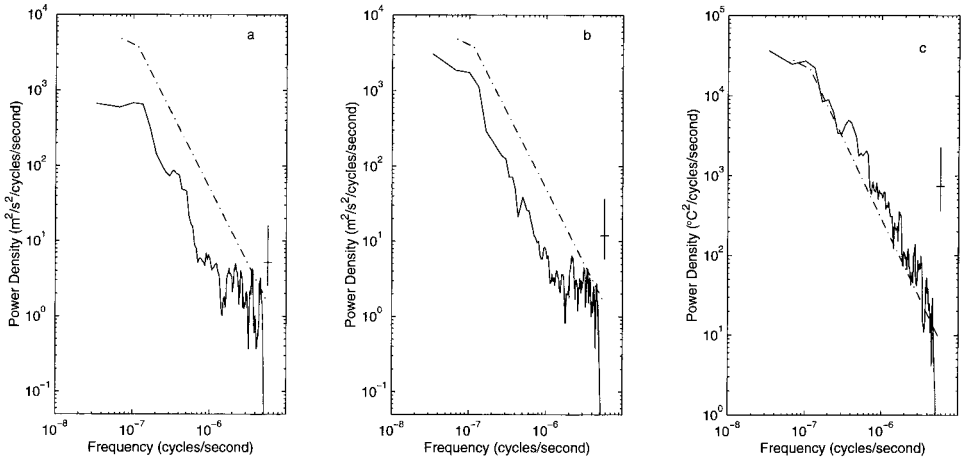

(iii)

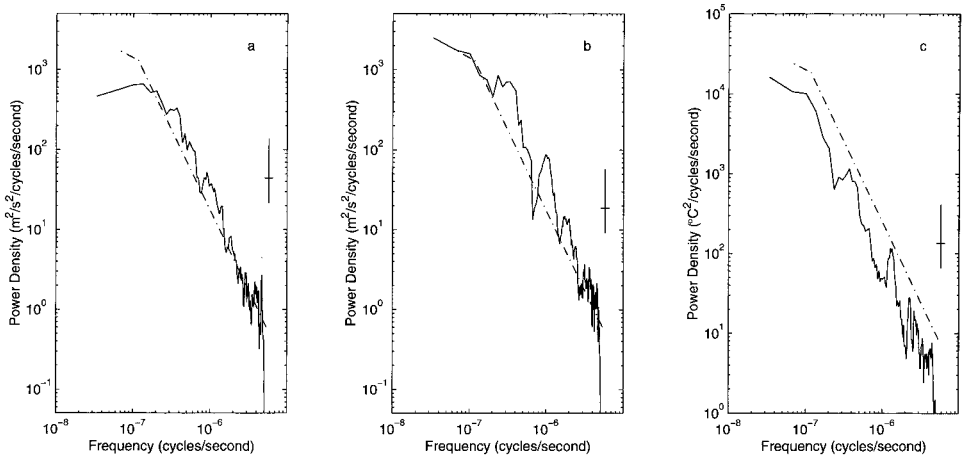

(iv)

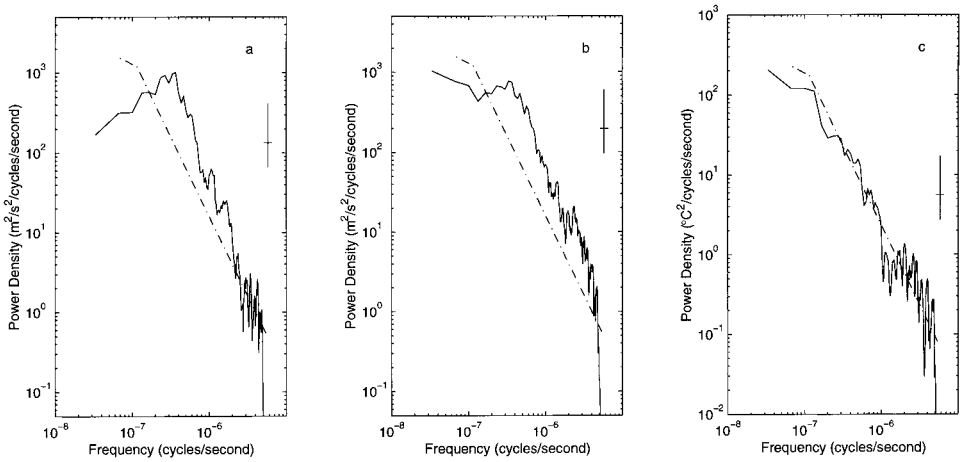

(v)

FIG. 15. (*Continued*)

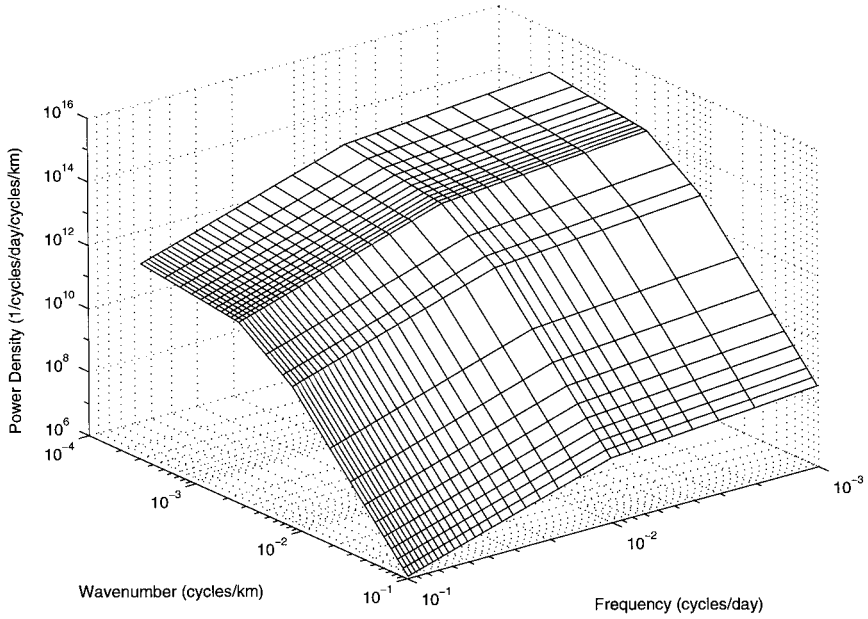

FIG. 16. The universal frequency and wavenumber spectrum for the stream function $\Phi(k, l, \omega, n, \phi, \lambda)/I(\phi, \lambda)$, which is identical for each mode.

white noise atmospheric forcing at periods longer than one week produced an open ocean frequency spectrum proportional to ω^{-2} at periods from a few days to about 150 days. At periods longer than a year, the frequency spectrum of the ocean is more nearly white because negative feedbacks become important [see Frankignoul and Müller (1979); Willebrand et al. (1980)]. The latter found that the ocean response should be primarily barotropic at periods between the inertial period and about 300 days, a result in conflict with the observations and hence with our model.

The present work can be improved and modified in a large number of ways, and we anticipate that ultimately regional spectral models will emerge, perhaps described in terms of their deviations from this more global one. Near the western boundary currents, the barotropic mode dominates (Wunsch 1997); the effect of mean flow cannot be neglected and significant differences exist between the energy level of zonal and meridional components of horizontal velocity. The frequency and wavenumber spectral shape near the western boundary is also different from that in the interior ocean (Stammer 1997). In areas close to the equator, high modes become more important (Eriksen 1981; Wunsch 1997) and, as mentioned, high latitudes may also be dominated by barotropic motions. Topography on all scales must also introduce strong inhomogeneities of many types.

Within the ocean interior, evidence does exist that some of the energy (10%–40% depending on location, but diminishing poleward) is consistent with anisotropically propagating linear Rossby waves (Zang and Wunsch 1999). More generally, there are real anisotropies as a function of frequency; Zang (2000) found in the North Pacific that the energy of westward-going motions was higher than that of eastward-going ones by a factor of 3 at low frequencies and long wavelengths. Finally, Stammer and Wunsch (1999) identified regional trends in surface eddy kinetic energy over a four year TOPEX/Poseidon record and this temporal nonstationarity is also excluded in the model.

Despite all its shortcomings, the model can be used quantitatively for a number of applications. Two examples are now provided.

a. An unobserved wavenumber spectrum: Horizontal velocity

The wavenumber spectrum of horizontal velocity in the ocean is not normally determinable, requiring for direct calculation, elaborate current meter arrays. Here we will estimate it from the measurements of other quantities that were available to us.

Figure 17 shows the estimate of the zonal-wavenumber spectrum of zonal and meridional component of horizontal velocity, based on the estimated $\Phi(k, l, \omega, n, \phi, \lambda)$. The zonal-wavenumber spectrum of zonal velocity is proportional to $k^{-1/2}$ at wavelengths longer than 400 km, $k^{-5/2}$ at wavelengths between 100 km and 400 km, and k^{-4} at wavelengths shorter than 100 km. The zonal-wavenumber spectral shape of the zonal velocity is similar to the observed zonal-wavenumber spectral shape of sea surface height and temperature and discussed in section 4. The zonal-wavenumber spectrum of meridional velocity is nearly white, with a weak maximum at wavelengths near 400 km and has a slope of $+1.5$ and -0.5

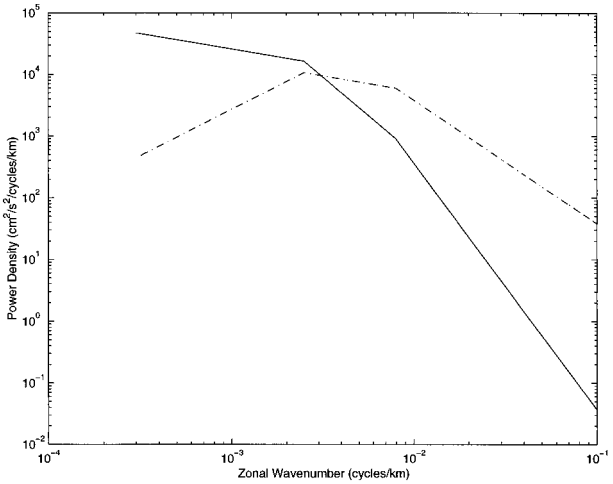

FIG. 17. Zonal-wavenumber spectrum of zonal velocity (solid line) and meridional velocity (dash–dotted line). The total kinetic energy is 100 $cm^2\ s^{-2}$. Note that zonal-wavenumber spectral shape of zonal velocity is similar to zonal-wavenumber spectral shape of temperature and sea surface height which is displayed in section 4.

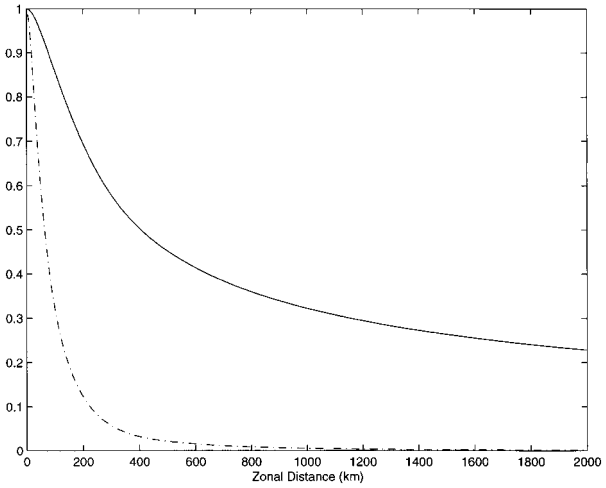

FIG. 19. The normalized $\sigma^2_{\bar{\theta}}(L, n, \lambda, \phi)$ (solid line) and $\sigma^2_{\bar{v}}(L, n, \lambda, \phi)$ (dash–dot line) as a function of L; $\sigma^2_{\bar{\theta}}(L, n, \lambda, \phi)$ and $\sigma^2_{\bar{v}}(L, n, \lambda, \phi)$ are normalized by $\sigma^2_{\bar{\theta}}(L = 0, n, \lambda, \phi)$ and $\sigma^2_{\bar{v}}(L = 0, n, \lambda, \phi)$, respectively.

at wavelengths longer and shorter than 400 km, respectively. The most conspicuous feature of Fig. 17 is that the zonal-wavenumber spectrum of zonal velocity is redder than the zonal-wavenumber spectrum of meridional velocity. The ratio of the zonal-wavenumber spectrum of zonal velocity to the zonal-wavenumber spectrum of meridional velocity is proportional to k^{-2}.

A rationalization of the relationship among the wavenumber spectra of sea surface height, zonal velocity, and meridional velocity follows from geostrophy. For large-scale and low frequency variability in the ocean, the horizontal momentum equation is dominated by the geostrophic balance:

$$fv = g\frac{\partial \eta}{\partial x}, \tag{34}$$

$$fu = -g\frac{\partial \eta}{\partial y}, \tag{35}$$

where η is the seasurface elevation. A Fourier transform of Eq. (34) with respect to x gives

$$\tilde{f}_v(k) = \frac{i2\pi kg}{f}\tilde{f}_\eta(k), \tag{36}$$

where $\tilde{f}_v(k)$ and $\tilde{f}_\eta(k)$ are the Fourier transform of meridional velocity and sea surface height. Define $F_v(k)$ and $F_\eta(k)$ to be the zonal-wavenumber spectrum of meridional velocity and sea surface height; then,

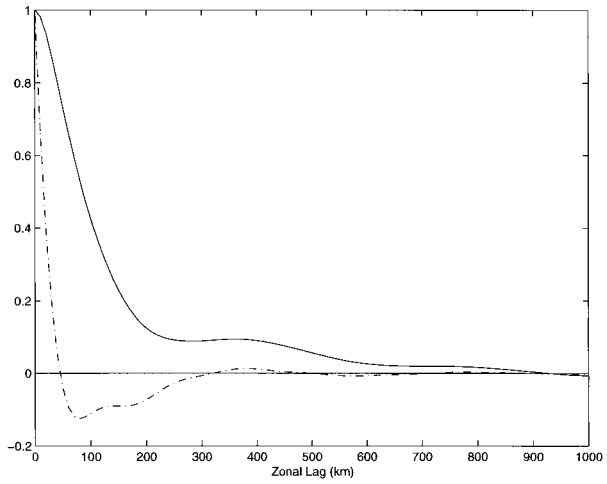

FIG. 18. Autocorrelation of zonal velocity (solid line) and meridional velocity (dash–dotted line) as a function of zonal separation distance. Zonal autocorrelation of temperature is the same as zonal autocorrelation of zonal velocity.

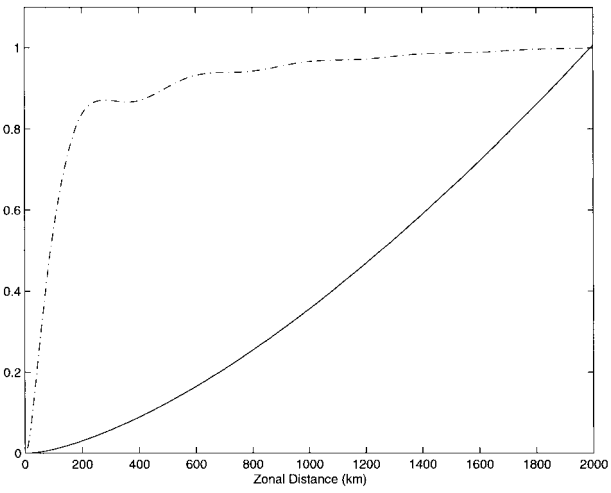

FIG. 20. The normalized $\sigma^2_\Theta(L, n, \lambda, \phi)$ (solid line) and $\sigma^2_V(L, n, \lambda, \phi)$ (dash–dot line) as a function of L; $\sigma^2_\Theta(L, n, \lambda, \phi)$ and $\sigma^2_V(L, n, \lambda, \phi)$ are normalized by $\sigma^2_\Theta(L = 2000, n, \lambda, \phi)$ and $\sigma^2_V(L = 2000, n, \lambda, \phi)$ respectively.

TABLE 2. Standard deviation of volume flux (Sv $\equiv 10^6$ m^3 s^{-1}), average temperature, and heat content for the first three modes and the standard deviation of the total variability at 24°N in the North Atlantic.

	σ_V (0–2000 m) (Sv)	$\sigma_{\bar{\theta}}$ (1000–2000 m) (°C)	σ_Θ (1000–2000 m) (J m^{-1})
$n = 0$	2.6		
$n = 1$	1.8	0.012	2.5×10^{14}
$n = 2$	1.0	0.022	4.4×10^{14}
total	3.4	0.025	5.1×10^{14}

$$\frac{F_v(k)}{F_\eta(k)} = \frac{\langle |\tilde{f}_v(k)|^2 \rangle}{\langle |\tilde{f}_\eta(k)|^2 \rangle} \propto k^2, \tag{37}$$

and

$$\frac{F_u(k)}{F_\eta(k)} \propto k^0, \tag{38}$$

which means that zonal velocity and sea surface height have the same zonal-wavenumber spectral shape. The relationship between the zonal-wavenumber spectral shape of zonal velocity and meridional velocity can be obtained from Eqs. (37) and (38) and

$$\frac{F_u(k)}{F_v(k)} \propto k^{-2} \tag{39}$$

$$\frac{F_u(l)}{F_v(l)} \propto l^2, \tag{40}$$

showing that the meridional-wavenumber spectrum of meridional velocity is more red than that for zonal velocity. This above discussion is for sea surface currents only. If the spectral shape is independent of depth, Eqs. (39) and (40) can be applied at any depth.

b. Covariance functions

For some calculations, for example, for mapmaking and interpolation, it is convenient to work in the temporal and/or spatial domains, and one seeks the covariance functions implied by the estimated power density spectra. The Fourier transform of the wavenumber (frequency) spectrum is the spatial (temporal) covariance. For example, the zonal autocovariance of temperature for each vertical mode is

$$R_\theta(r_x, n, \phi, \lambda, z) = f^2 G_n^2(z) \left(\frac{\partial \theta_0}{\partial z}\right)^2 \int_{-\infty}^{+\infty} \int_{-\infty}^{+\infty} \int_{-\infty}^{+\infty} \Phi(k, l, \omega, n, \phi, \lambda) \cos(2\pi k r_x)\, dk\, dl\, d\omega. \tag{41}$$

The autocovariance of temperature and horizontal velocity as a function of zonal separation distance is displayed in Fig. 18. It shows an exponential decay with *e*-folding spatial scales of about 150 km. The zonal autocovariance function of meridional velocity (Fig. 18) has a zero crossing near 50 km. A striking feature is that the autocovariance of zonal velocity is higher than that of meridional velocity for the same zonal separation distance. These results are consistent with well-known results from the theory of three-dimensional homogeneous turbulence (Batchelor 1953) that the longitudinal velocity autocorrelation (autocorrelation of the velocity parallel to the separation vector) is always higher than the lateral velocity autocorrelation. Middleton and Garrett (1986) showed that Batchelor's result could be readily extended to two-dimensional turbulence. Based on drifter data, they obtained an estimate of the correlation of transverse velocity and found it had a zero crossing at 32 km.

c. Estimating the variability of volume flux and section heat content

Volume and heat transport in the ocean are often estimated from hydrographic measurements (e.g., Wunsch 1996). These fluxes, and related quantities vary with time, having values dependent upon the lengths of hydrographic sections and the areas covered (e.g., for heat content). Here we estimate the expected variability of heat content and volume flux due to mesoscale eddies.

Suppose that a zonal hydrographic section of length L terminates at land at each end. The variance of the average temperature for each vertical mode in the region bounding the hydrographic section is

$$\sigma_{\bar{\theta}}^2(L, n, \lambda, \phi) = \left(\frac{1}{h} \int_{h_1}^{h_2} \frac{\partial \theta_0}{\partial z} G_n(z)\, dz\right)^2 \int_{-\infty}^{+\infty} \int_{-\infty}^{+\infty} \int_{-\infty}^{+\infty} f^2 \Phi(k, l, \omega, n, \lambda, \phi) W(k, L)\, d\omega\, dk\, dl, \tag{42}$$

and the variance of the average meridional velocity is

$$\sigma_{\bar{v}}^2(L, n, \lambda, \phi) = \left(\frac{1}{h}\int_{h_1}^{h_2} F_n(z)\, dz\right)^2 \int_{-\infty}^{+\infty}\int_{-\infty}^{+\infty}\int_{-\infty}^{+\infty} 4\pi^2 k^2 \Phi(k, l, \omega, n, \lambda, \phi) W(k, L)\, d\omega\, dk\, dl, \quad (43)$$

where h_1 and h_2 are the depths of the lower and upper boundary of the hydrographic section; $h = h_2 - h_1$ and

$$W(k, L) = \frac{\sin^2(\pi k L)}{(\pi k L)^2}; \quad (44)$$

$W(k, L)$ arises from the horizontal averaging. In (42) and (43) $\sigma_{\bar{\theta}}^2(L, n, \lambda, \phi)$ and $\sigma_{\bar{v}}^2(L, n, \lambda, \phi)$ depend on location as well as the zonal length L. Our first concern is how they depend on the zonal length L. At each site $\sigma_{\bar{\theta}}^2(L, n, \lambda, \phi)$ and $\sigma_{\bar{v}}^2(L, n, \lambda, \phi)$ are normalized by their maximum values, $\sigma_{\bar{\theta}}^2(L = 0, n, \lambda, \phi)$ and $\sigma_{\bar{v}}^2(L = 0, n, \lambda, \phi)$. As displayed in Fig. 19, the normalized $\sigma_{\bar{\theta}}^2(L, n, \lambda, \phi)$ and $\sigma_{\bar{v}}^2(L, n, \lambda, \phi)$ decrease with L. Figure 19 shows that, as one expects, the longer the length of the hydrographic section, the less variable is the average temperature and the average meridional velocity. Here $\sigma_{\bar{v}}^2(L, n, \lambda, \phi)$ decreases with L much more rapidly than does $\sigma_{\bar{\theta}}^2(L, n, \lambda, \phi)$. For average temperature, half of the energy is filtered out when the zonal length is about 350 km; for average meridional velocity, 90% of the variance is removed due to filtering when the zonal distance is 200 km.

The variance of volume flux is

$$\sigma_V^2(L, n, \lambda, \phi) = h^2 L^2 \sigma_{\bar{v}}^2(L, n, \lambda, \phi), \quad (45)$$

and the variance of heat content is

$$\sigma_\Theta^2(L, n, \lambda, \phi) = \rho_0^2 c_p^2 h^2 L^2 \sigma_{\bar{\theta}}^2(L, n, \lambda, \phi), \quad (46)$$

where ρ_0 is the density of the basic state and c_p is the specific heat. Note that $\sigma_\Theta^2(L, n, \lambda, \phi)$ and $\sigma_V^2(L, n, \lambda, \phi)$ do not simply increase with L^2 (Fig. 20). The variance of volume flux increases rapidly as L increases from 0 to 200 km, then it increases very slowly. As L increases from 200 to 2000 km, the variance of volume flux only increases by about 15% because the zonal length scale of mesoscale eddies is about 200 km. Because the zonal length scale of temperature is much larger than that of meridional velocity, the variance of heat content always increases with L.

Variances of volume transport and heat content depend on location, too. As a representative result, the variance of the volume flux and heat content for the hydrographic section along 24°N in the North Atlantic is estimated (see, e.g., Roemmich and Wunsch 1984; Parrilla et al. 1994; Arbic and Owens 2001). For the volume transport, the vertical integration is chosen to be from the surface to 2000 m, while for heat content (temperature), the vertical integration is taken from 1000 to 2000 m because the signal-to-noise ratio for temperature is largest within this depth range. The standard deviation of volume flux, average temperature and heat content for this particular hydrographic section are listed in Table 2, which shows that the variability of barotropic and baroclinic volume fluxes are approximately the same. For average temperature, the variability in the second baroclinic mode is larger than that in the first baroclinic mode. These results are all consistent with the ad hoc calculations of Ganachaud (1999) and Arbic and Owens (2001).

Many other applications are possible, including, for example, coherence estimates, and applications to array design, estimation of Lagrangian particle statistics, etc. Some of these problems are worked out in Zang (2000).

Acknowledgments. We thank N. Hogg, B. Owens, and D. Stammer for comments. Suggestions by C. Garrett and an anonymous reviewer helped improve the presentation of this work. Supported in part by National Science Foundation through Grants OCE-9529545, Jet Propulsion Laboratory, California Institute of Technology through Contract 958125, and University of Texas-Austin through Contract UTA-98-0222.

APPENDIX A

Vertical Representation

Rigid-lid upper and lower boundary conditions are used here:

$$\omega(z) = 0, \qquad z = 0, \qquad -h \quad (A1)$$

or

$$G_n(z) = 0, \qquad z = 0, \qquad -h \quad (A2)$$

Here the depth of the ocean, h, is assumed constant and $h = 4500$ m. The solutions of the vertical structure for baroclinic modes are obtained first and the barotropic mode is explicitly added later.

The solution to (4) is (GM)

$$G_n(z) = A_n J_0\left(\frac{N_0 r_n}{a} e^{az}\right) + B_n Y_0\left(\frac{N_0 r_n}{a} e^{az}\right), \quad n \geq 1, \quad (A3)$$

where $J_0(z)$ and $Y_0(z)$ are the Bessel function of the first kind. Boundary conditions require

$$J_0(\xi_{-h}) Y_0(\xi_0) - J_0(\xi_0) Y_0(\xi_{-h}) = 0 \quad \text{and} \quad (A4)$$

$$B_n = \frac{J_0(\xi_0)}{Y_0(\xi_0)} A_n, \quad (A5)$$

where,

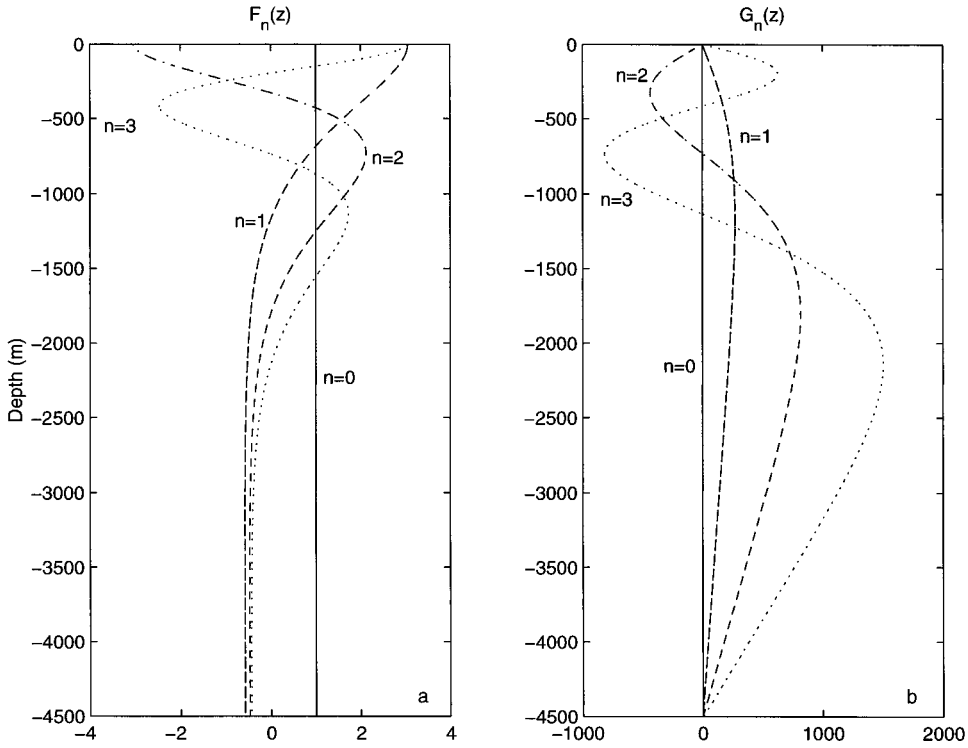

FIG. A1. The vertical eigenfunctions $F_n(z)$ and $G_n(z)$ for modes $0 \le n \le 3$ from the analytical $N(z)$ profile.

$$\xi = \frac{N_0 r_n}{a} e^{az}, \qquad \xi_0 = \frac{N_0 r_n}{a}, \qquad \xi_{-h} = \frac{N_0 r_n}{a} e^{-ah}. \quad \text{(A6)}$$

Defining

$$W_n(z) = J_0(\xi) - \frac{J_0(\xi)}{Y_0(\xi)} Y_0(\xi), \quad \text{(A7)}$$

then

$$F_n(z) = -\frac{1}{r_n^2}\frac{dG_n(z)}{dz} = -\frac{A_n}{r_n^2}\frac{dW_n(z)}{dz}. \quad \text{(A8)}$$

The vertical normalization is taken as

$$\frac{1}{h}\int_{-h}^{0} F_n^2(z)\, dz = 1, \quad \text{(A9)}$$

and the normalized vertical eigenfunctions are

$$F_n(z) = -\sqrt{\frac{h}{ab_n}}\frac{dW_n(z)}{dz} = a\xi\sqrt{\frac{h}{ab_n}}\left[J_1(\xi) - \frac{J_0(\xi_0)}{Y_0(\xi_0)} Y_1(\xi)\right], \quad n \ge 1 \quad \text{(A10)}$$

$$G_n(z) = \sqrt{\frac{h}{ab_n}} r_n^2 W_n(z), \qquad n \ge 1 \quad \text{(A11)}$$

where,

$$b_n = \int_{\xi_{-1}}^{\xi_0} \xi W_n^2(\xi)\, d\xi = \frac{2}{\pi^2}[Y_0^{-2}(\xi_0) - Y_0^{-2}(\xi_{-1})]. \quad \text{(A12)}$$

For the barotropic mode, that is, $n = 0$,

$$r_0 = 0, \qquad F_0(z) = 1, \qquad G_0(z) = 0, \quad \text{(A13)}$$

and are independent of depth.

The vertical eigenfunctions satisfy the orthonormality conditions

$$\frac{1}{h}\int_{-h}^{0} F_m(z)F_n(z)\, dz = \delta_{nm}, \quad \text{(A14)}$$

$$\frac{1}{h}\int_{-h}^{0} N^2(z)G_m(z)G_n(z)\, dz = r_n^2\delta_{nm}, \quad \text{(A15)}$$

where δ_{nm} is the Kronecker delta function. Note that the function $F_n(z)$ is nondimensional and the units of $G_n(z)$ are s^2m^{-1}. The $F_n(z)$ and $G_n(z)$ are plotted in Fig. A1 for $0 \le n \le 3$. An important property in Fig. A1 is the near-surface intensification of $F_n(z)$ for $n \ne 0$. Because the vertical structure of the horizontal kinetic energy is proportional to $F_n^2(z)$, the vertical structure of baroclinic horizontal kinetic energy will correspondingly show a near-surface intensification.

APPENDIX B

Characteristic Function

The characteristic functions for pressure, zonal velocity, etc., are

$$\tilde{p}(k, l, \omega, z, n) = \rho_0 f F_n(z), \tag{B1}$$

$$\tilde{u}(k, l, \omega, z, n) = -i2\pi l F_n(z), \tag{B2}$$

$$\tilde{v}(k, l, \omega, z, n) = i2\pi k F_n(z), \tag{B3}$$

$$\tilde{w}(k, l, \omega, z, n) = i2\pi\omega f G_n(z), \tag{B4}$$

$$\tilde{\rho}(k, l, \omega, z, n) = -\frac{\rho_0 f}{g} N^2(z) G_n(z), \tag{B5}$$

$$\tilde{\zeta}(k, l, \omega, z, n) = -f G_n(z), \tag{B6}$$

$$\tilde{\theta}(k, l, \omega, z, n) = f\frac{\partial\theta_0}{\partial z} G_n(z). \tag{B7}$$

The vertical displacement ζ is here attributed to the vertical advection of the mean vertical temperature profile $\partial\theta_0/\partial z$,

$$\zeta(x, y, z, t) = -\frac{\theta(x, y, z, t)}{\partial\theta_0/\partial z}. \tag{B8}$$

APPENDIX C

Final Model Spectra

Given $\Phi(k, l, \omega, n, \phi, \lambda)$, one can estimate the model spectrum of any variable at any place. A few useful examples are given here.

The total kinetic energy per unit surface area for each mode is

$$K_E(n) = \int_{-\infty}^{+\infty}\int_{-\infty}^{+\infty}\int_{-\infty}^{+\infty} 2\pi^2(k^2 + l^2)\Phi(k, l, \omega, n, \phi, \lambda)\, dk\, dl\, d\omega = 5.9 \times 10^{31} I(\phi, \lambda) E_0(n) \quad [\mathrm{m}^2/\mathrm{s}^2]. \tag{C1}$$

The potential energy per unit surface area for each mode is

$$P_E(n, \phi, \lambda) = \frac{1}{2R_n^2}\int_{-\infty}^{+\infty}\int_{-\infty}^{+\infty}\int_{-\infty}^{+\infty}\Phi(k, l, \omega, n, \phi, \lambda)\, dk\, dl\, d\omega = \frac{7.8 \times 10^{40} I(\phi, \lambda) E_0(n)}{R_n^2} \quad [\mathrm{m}^2/\mathrm{s}^2]. \tag{C2}$$

Therefore, the ratio of kinetic energy to potential energy per unit surface area for the first baroclinic mode

$$\frac{K_E(1, \phi, \lambda)}{P_E(1, \phi, \lambda)} = 7.6 \times 10^{-10} R_1^2. \tag{C3}$$

If we take $f = 10^{-4}\ \mathrm{s}^{-1}$, which is the value of f at midlatitude, (6) gives $R_1 = 2500$ m. Then

$$\frac{K_E(1, \phi, \lambda)}{P_E(1, \phi, \lambda)} = 0.48. \tag{C4}$$

The zonal-wavenumber spectrum of sea surface height is

$$\Upsilon_\eta^{(1)}(k, \phi, \lambda) = \sum_{n=0}^{n=2}\frac{f^2 F_n^2(z=0)}{g^2}\int_{-\infty}^{+\infty}\int_{-\infty}^{+\infty}\Phi(k, l, \omega, n, \phi, \lambda)\, dl\, d\omega = 9.2 \times 10^{15}\sin^2\phi I(\phi, \lambda) B_1(k) \quad [\mathrm{m}^2/(\text{cycles/meter})]. \tag{C5}$$

The meridional-wavenumber spectrum of sea surface height is identical.

The variance of sea surface height is

$$\sigma_\eta^2(\phi, \lambda) = \sum_{n=0}^{n=2}\frac{f^2 F_n^2(z=0)}{g^2}\int_{-\infty}^{+\infty}\int_{-\infty}^{+\infty}\int_{-\infty}^{+\infty}\Phi(k, l, \omega, n, \phi, \lambda)\, dk\, dk\, d\omega = 5.0 \times 10^{32}\sin^2\phi I(\phi, \lambda) \quad [\mathrm{m}^2]. \tag{C6}$$

The zonal-wavenumber spectrum of temperature

$$\Upsilon_\eta^{(1)}(k, z, \phi, \lambda) = \sum_{n=0}^{n=2} f^2 G_n^2(z)\left(\frac{\partial\theta_0}{\partial z}\right)^2\int_{-\infty}^{+\infty}\int_{-\infty}^{+\infty}\Phi(k, l, \omega, n, \phi, \lambda)\, dl\, d\omega = 6.0 \times 10^{16}\sin^2\phi I(\phi, \lambda)[G_1^2(z) + 0.5 \times G_2^2(z)]\left(\frac{\partial\theta_0}{\partial z}\right)^2 B_1(k) \quad [^\circ\mathrm{C}^2/(\text{cycles/meter})], \tag{C7}$$

where the units of $G_n^2(z)$ are $s^4\ m^{-2}$, the units of $\partial\theta_0/\partial z$ are °C/m, and the meridional spectrum is identical.

The frequency spectrum of sea surface height

$$\Upsilon_{\eta}^{(1)}(\omega, \phi, \lambda) = \sum_{n=0}^{n=2} \frac{f^2 F_n^2(z=0)}{g^2} \int_{-\infty}^{+\infty}\int_{-\infty}^{+\infty} \Phi(k, l, \omega, n, \phi, \lambda)\, dk\, dl = 9.7 \times 10^{24} \sin^2\phi I(\phi, \lambda) D_1(\omega) \quad [m^2/(\text{cycles/second})]. \tag{C8}$$

The frequency spectrum of zonal and meridional velocity

$$\Upsilon_{u}^{(1)}(\omega, z, \phi, \lambda) = \Upsilon_{v}(\omega, z, \phi, \lambda) = 1.1 \times 10^{24}[F_0^2(z) + F_1^2(z) + 0.5 \times F_2^2(z)] D_1(\omega), \tag{C9}$$

in the units of $(m^2/s^2)/(\text{cycles/second})$.

The frequency spectrum of temperature

$$\Upsilon_{\theta}^{(1)}(\omega, z, \phi, \lambda) = 6.3 \times 10^{25} \sin^2\phi I(\phi, \lambda)[G_1^2(z) + 0.5 \times G_2^2(z)] \times \left(\frac{\partial\theta_0}{\partial z}\right)^2 D_1(\omega) \quad [°C^2/(\text{cycles/second})], \tag{C10}$$

where the units of $G_n^2(z)$ are $s^4\ m^{-2}$ and the units of $\partial\theta_0/\partial z$ are °C/m.

REFERENCES

Arbic, B., and B. Owens, 2001: Climatic warming of Atlantic Intermediate Waters. *J. Climate,* **14,** 4091–4108.

Batchelor, G. K., 1953: *The Theory of Homogeneous Turbulence*. Cambridge University Press, 197 pp.

Charney, J. G., 1971: Geostrophic turbulence. *J. Atmos. Sci.,* **28,** 1087–1095.

Chelton, D. B., R. A. de Szoeke, M. G. Schlax, K. El Naggar, and N. Siwertz, 1998: Geographical variability of the first baroclinic Rossby radius of deformation. *J. Phys. Oceanogr.,* **28,** 433–460.

Eriksen, C. C., 1981: Deep currents and their interpretation as equatorial waves in the western Pacific Ocean. *J. Phys. Oceanogr.*, **11,** 48–70.

Fjörtoft, R., 1953: On the changes in the spectral distribution of kinetic energy for two-dimensional, nondivergent flow. *Tellus,* **5,** 225–230.

Frankignoul, C., and K. Hasselmann, 1977: Stochastic climate models. Part 2, Application to sea-surface temperature anomalies and thermocline variability. *Tellus,* **29,** 289–305.

——, and P. Müller, 1979: Quasi-geostrophic response of an infinite beta-plane ocean to stochastic forcing by the atmosphere. *J. Phys. Oceanogr.*, **9,** 104–127.

Fu, L.-L., and G. Flierl, 1980: Nonlinear energy and enstrophy transfers in a realistically stratified ocean. *Dyn. Atmos. Oceans,* **4,** 219–246.

Fukumori, I., R. Raghunath, and L.-L. Fu, 1998: Nature of global large-scale sea level variability in relation to atmospheric forcing: A modeling study. *J. Geophys. Res.,* **103,** 5493–5312.

Ganachaud, S. A., 1999: Large-scale oceanic circulation and fluxes of freshwater, heat, nutrients and oxygen. Ph.D. thesis, MIT/WHOI Joint Program, 266 pp.

Garrett, C., and W. Munk, 1972: Space–time scales of internal waves. *Geophys. Fluid Dyn.,* **2,** 225–264.

Gill, A. E., 1982: *Atmosphere–Ocean Dynamics.* Academic Press, 662 pp.

Gille, S. T., and S. G. Llewellyn-Smith, 2000: Velocity probability density functions from altimetry. *J. Phys. Oceanogr.*, **30,** 125–136.

Gilson, J., D. Roemmich, B. Cornuelle, and L.-L. Fu, 1998: The relationship of TOPEX/POSEIDON altimetric height to steric height and circulation in the North Pacific. *J. Geophys. Res.*, **103,** 27 947–27 965.

Hasselmann, K., 1976: Stochastic climate models. Part I, theory. *Tellus*, **28,** 473–485.

Kraichnan, R. H., 1967: Inertial ranges in two dimensional turbulence. *Phys. Fluids*, **10,** 1417–1423.

Le Traon, P. Y., F. Nadal, and N. Ducet, 1998: An improvement mapping method of multi-satellite altimeter data. *J. Atmos. Oceanic Technnol.,* **15,** 522–534.

Lilly, D. K., 1969: Numerical simulation of two-dimensional turbulence. *Phys. Fluids,* **12,** 240–249.

McWilliams, J. C., and H. H. S. Chow, 1981: Equilibrium geostrophic turbulence I: A reference solution in a β-plane channel. *J. Phys. Oceanogr.,* **11,** 921–949.

Middleton, J. F., and C. Garrett, 1986: A kinematic analysis of polarized eddy fields using drifter data. *J. Geophys. Res.,* **91,** 5094–5102.

Munk, W., P. F. Worcester, and C. Wunsch, 1996: *Ocean Acoustic Tomography.* Cambridge University Press, 433 pp.

Parrilla, G., A. Lavin, H. Bryden, M. Garcia, and R. Millard, 1994: Rising temperature in the subtropical North Atlantic Ocean over the past 35 years. *Nature,* **369,** 48–51.

Percival, D. B., and A. T. Walden, 1993: *Spectral Analysis for Physical Applications. Multitaper and Conventional Univariate Techniques.* Cambridge University Press, 583 pp.

Rhines, P. B., 1975: Waves and turbulence on a β-plane. *J. Fluid Mech.,* **69,** 417–443.

Roemmich, D., and C. Wunsch, 1984: Apparent changes in the climatic state of the deep North Atlantic Ocean. *Nature,* **307,** 447–450.

——, and B. Cornuelle, 1990: Observing the fluctuations of gyre-scale ocean circulation: A study of the subtropical South Pacific. *J. Phys. Oceanogr.,* **20,** 1919–1930.

Schmitz, W. J., Jr., 1978: Observations of the vertical distribution of low frequency kinetic energy in the western North Atlantic. *J. Mar. Res.,* **36,** 295–310.

——, 1988: Exploration of the eddy field in the mid-latitude North Pacific. *J. Phys. Oceanogr.,* **18,** 459–468.

Stammer, D., 1997: Global characteristic of ocean variability estimated from regional TOPEX/POSEIDON altimeter measurements. *J. Phys. Oceanogr.,* **27,** 1743–1770.

——, and C. Wunsch, 1999: Temporal changes in eddy energy of the oceans. *Deep-Sea Res.,* **46,** 77–108.

——, ——, and R. Ponte, 2000: De-aliasing of global high frequency barotropic motions in altimeter observations. *Geophys. Res. Lett.,* **8,** 1175–1178.

Tierney, C., J. Wahr, F. Bryan, and V. Zlotnicki, 2000: Short-period oceanic circulation: Implications for satellite altimetry. *Geophys. Res. Lett.,* **27,** 1255–1258.

Willebrand, J., S. G. H. Philander, and R. C. Pacanowski, 1980: The oceanic response to large-scale atmospheric disturbances. *J. Phys. Oceanogr.,* **10,** 411–429.

Wunsch, C., 1981: Low frequency variability in the sea. *Evolution of Physical Oceanography: Scientific Surveys in Honor of Henry Stommel,* B. A. Warren and C. Wunsch, Eds., The MIT Press, 342–374.

——, 1996: *The Ocean Circulation Inverse Problem.* Cambridge University Press, 442 pp.

——, 1997: The vertical partition of oceanic horizontal kinetic energy. *J. Phys. Oceanogr.*, **27,** 1770–1794.
——, 1999a: Where do ocean eddy heat fluxes matter? *J. Geophys. Res.*, **104,** 13 235–13 249.
——, 1999b: A summary of North Atlantic baroclinic variability. *J. Phys. Oceanogr.*, **29,** 3161–3166.
——, and D. Stammer, 1995: The global frequency-wavenumber spectrum of oceanic variability estimated from TOPEX/POSEIDON altimeter measurements. *J. Geophys. Res.*, **100,** 24 895–24 910.
——, and ——, 1998: Satellite altimetry, the marine geoid and the oceanic general circulation. *Ann. Rev. Earth Planet. Sci.*, **26,** 219–253.
Zang, X., 1998: Space and time scales of low frequency variability in the ocean. M.S. thesis, MIT/WHOI Joint Program, 120 pp.
——, 2000: Spectral description of low frequency oceanic variability. Ph.D. thesis, MIT/WHOI Joint Program, 187 pp.
——, and C. Wunsch, 1999: The observed dispersion relation for North Pacific Rossby wave motions. *J. Phys. Oceanogr.*, **29,** 2183–2190.